RESPONSE ANALYSIS OF THE FLOW-INDUCED VIBRATION
OF FLEXIBLE CYLINDERS TESTED AT CASTINE, MAINE
IN JULY AND AUGUST OF 1981

by

JEN-YI JONG

J. KIM VANDIVER

DEPARTMENT OF OCEAN ENGINEERING

MASSACHUSETTS INSTITUTE OF TECHNOLOGY

CAMBRIDGE, MASS.   02139

15 January 1983

ABSTRACT

A cable-strumming experiment was conducted at Castine,
Maine in July and August of 1981. 75-foot long sections of a
1.25-inch diameter cable, and a 1.631-inch diameter pipe were
subjected to vortex induced vibration. Seven biaxial pairs
of accelerometers were placed at different locations along
the cable, and the pipe. Acceleration at these seven
positions, as well as tension, tidal current velocity, and
drag force were simultaneously recorded. Current velocities
ranged from 0 to 2.4 feet/second. A numerical double
integration technique is presented in detail and used to
obtain the transverse and in-line displacements. Modal
identification is used to evaluate the motion in terms of the
individual natural modal coordinates of the cable. Lockin
and non-lockin examples are presented. Cross flow amplitudes
are typically twice that of the in-line vibration. In-line
response frequencies are typically twice that of the cross
flow.

ACKNOWLEDGEMENTS

TABLE OF CONTENTS

LIST OF FIGURES

LIST OF FIGURES

I

CHAPTER 1
INTRODUCTION

Marine risers, tension elements on TLP's, and hydrophone cables are all examples of structures subject to vortex-induced vibration. The response of the cylinder depends upon a complex interaction between the natural modes of the vibration and the vortex-shedding process.

The purpose of this research was to evaluate the in-line and cross-flow displacements of long flexible cylinders from acceleration data obtained in field tests. Individual modal amplitudes were to be determined for in-line and cross-flow response for both lock-in and non-lock-in conditions. Experiments were performed on long flexible cylinders 75 feet in length which were exposed to uniform current ranging from 0 to 2.4 feet/second. Measurements taken included current, drag, tension and biaxial acceleration at seven locations along the test cylinders.

The angular orientations of the biaxial accelerometers were initial unknowns which had to be resolved by evaluation of the gravitational acceleration components recorded with the data. Once the orientation was established the horizontal (in-line) and vertical (cross-flow) vector acceleration components were obtained. A numerical double integration technique was developed to determine the vector displacement time histories at the seven measurement locations. The theoretical mode shapes of uniform cables, and beams under tension, with pinned ends, are simple sinusoids. By a least squares error minimization technique, it was possible to evaluate the individual modal contributions for in-line and cross-flow motions, and for lock-in and non-lock-in conditions. In other words, the vector displacement response was reduced to the separate time histories of the natural coordinates of the individual contributing modes. The data processing methodologies are

1

described and typical results are presented. Two and one half hour records of drag coefficient, current, and RMS displacement were calculated and are presented.

CHAPTER 2

THE EXPERIMENT

2.1 Test Site

The site chosen for the experiment, shown in Fig. 1 was
a sandbar located at the mouth of Holbrook Cove near Castine
Maine. This was the same site used in previous experiments
in 1975 and 1976 by Vandiver, Mazel and Kan (12,18). At low
tide, the sandbar was exposed allowing easy access to the
test equipment while at high tide it was covered by about 10
feet of water. The test section was oriented normal to the
direction of the current which varied from 0 to 2.4 ft/s over
the tidal cycle with only small spatial differences over the
section length at any given moment.

The data taking station for the experiment was the R/V
Edgerton chartered from the MIT Sea Grant Program. The
Edgerton was moored for the duration of the experiment
approximately 300 ft. from the sandbar and connected to the
instruments on the sandbar by umbilicals.

Prior to the data taking part of the experiment, several
days were needed to prepare the site. A foundation for the
experiment was needed to anchor the supports that were to
hold the ends of the test cylinders. To accomplish this, six
4.5 inch diameter steel pipes were water jetted into the
sandbar utilizing the fire pump aboard the Edgerton. These
six pipes were made of two, five foot sections joined by
couplings so that the overall length of each was 10.0 feet.
In addition, one 2.0 inch steel pipe, 6 feet long, was jetted
into the sandbar to be used as a current meter mount. Fig. 2
shows a schematic diagram of the experiment test section.

2.2 Drag Measuring System

A load cell mounted at one end of the test cylinder
measured the horizontal shear force on one end of the test
cylinder. The cylinder and its supports were symmetric, and
therefore the measured force was one half the total drag
force on the cylinder. Mean drag force was measured. The

CHANNEL
350 YDS.

N

SANDBAR

SITE
30 YDS.

MLW

FLOOD

MHW

EBB

YDS.
0   50

PLAN

N   LONG
68° 48' 04" R.0

CASTINE

BROOKS-
VILLE

44° 22' 38" N

LAT

YDS.
0   1000

FROM NOS CHART 13309
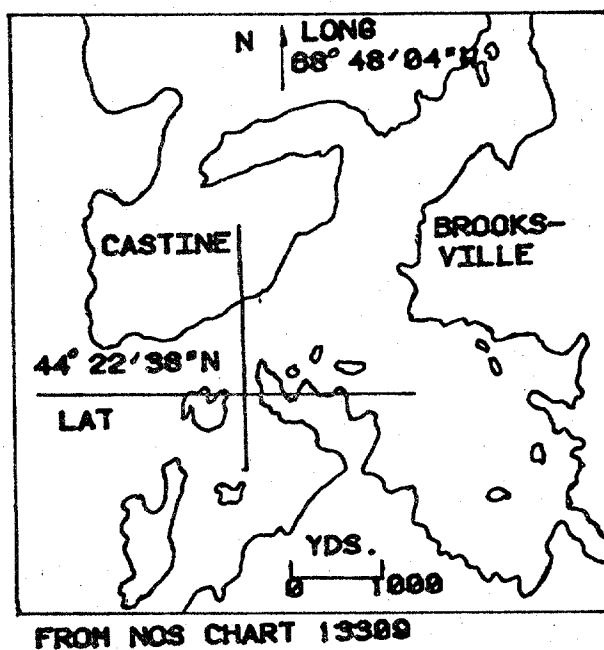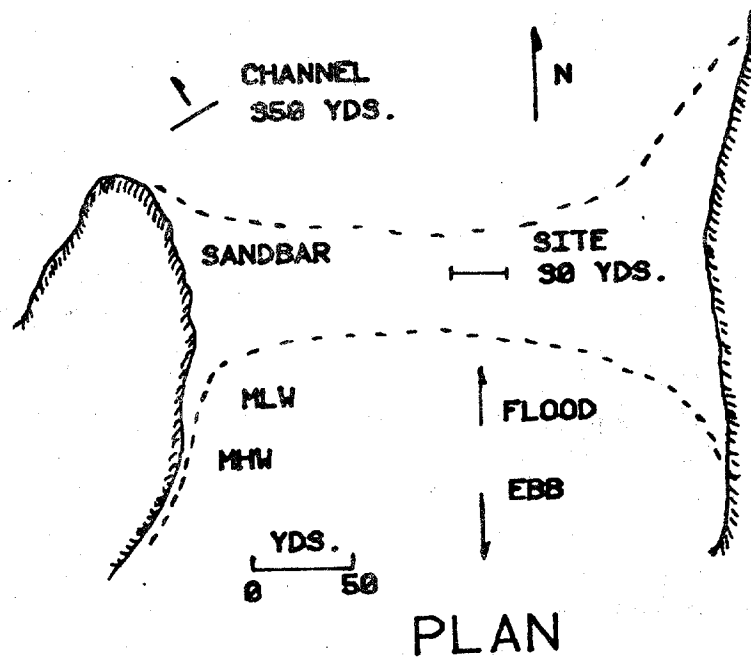
FIG. 1   THE EXPERIMENT SITE

4
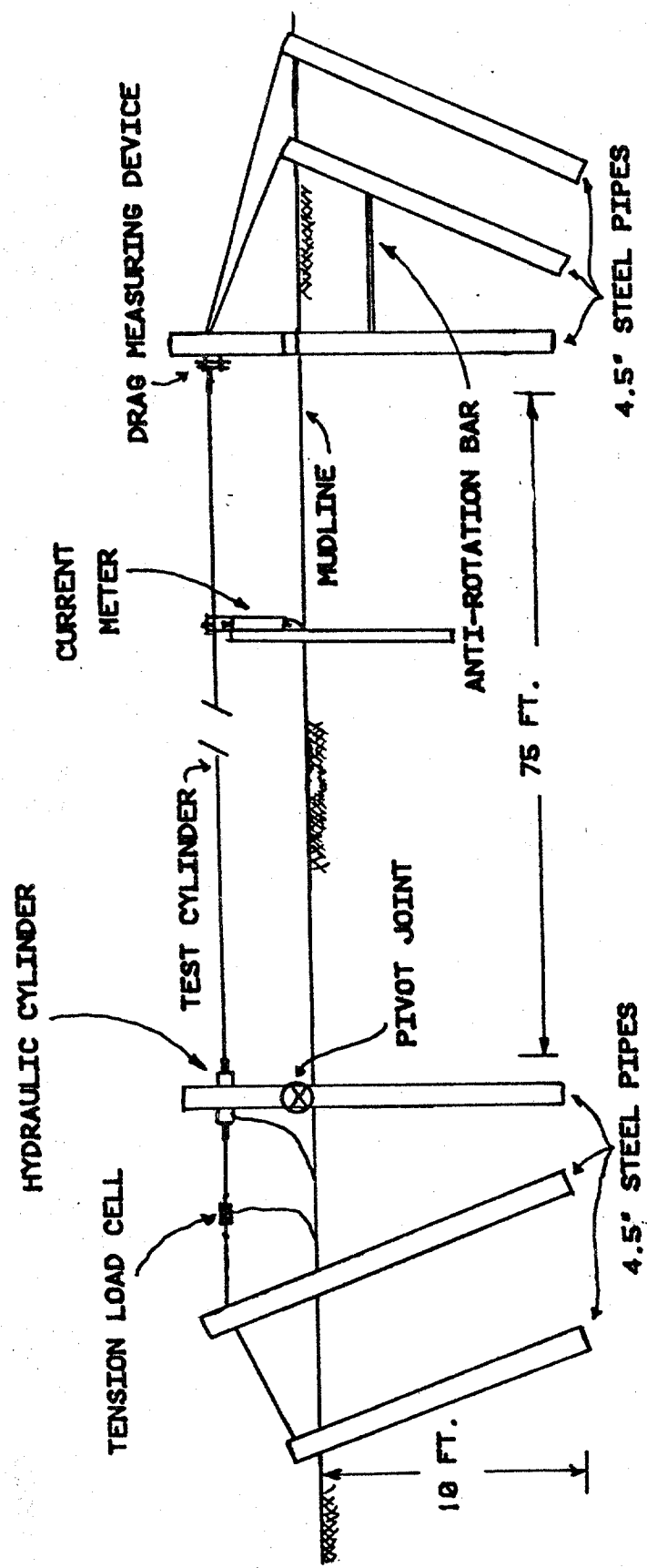
FIG. 2 SCHEMATIC DIAGRAM OF THE EXPERIMENT

TEST SECTION

5

mechanical details of the drag measuring mechanism way be
found in the thesis by J.McGlothlin. The load cell was a
Sensotec Model 41, packaged for underwater use. The signal
from the load cell traveled through wires in the test
cylinders and through the umbilical to the Edgerton where it
was conditioned and recorded.

2.3 Current Measuring System

The current was measured by a Neil Brown Instrument
Systems DRCM -2 Acoustic Current Meter located 12.5 feet from
the west end of the test cylinder and 2 feet upstream. It
was set so that it determined the current at the level of the
test cylinders. Signals from the current meter traveled
through umbilicals to the Edgerton where they were monitored
and recorded. In addition, a current meter traverse was
performed using an Endeco current meter to determine the
spatial differences in current along the test section. The
current was found to be spatially uniform to within + or -
3.0% from end to end for all current speeds above 0.5 feet
per second.

2.4 Tension Measuring System

The tension measuring and adjusting system was located
at the east end of the experiment test section. Extensions
were made to the two inner water jetted posts at this end.
As shown in the diagram, a 5-foot extension was made to the
center post and a 3-foot extension was made to the inner most
post. What made this 3-foot extension different from the
rest was that its attachment to the jetted pipe at the
mudline was a pin connection as compared to the standard pipe
couplings used on the other extensions. This pin connection
gave it the ability to pivot in the plane of the posts. Onto
this pivoting post, a hydraulic cylinder was mounted,
horizontally, 2.5 feet above the mudline. The test cylinder
was connected at one end to this hydraulic cylinder and at
the other end to the drag measuring device. The test
cylinder was attached 2.5 feet above the mudline, a
sufficient distance to avoid any boundary layer effects

6

caused by the sandbar. A cable ran from the back of the hydraulic cylinder to a Sensotec Model RM In-Line load cell which was anchored at the other end to the center post. In this way, the force on the test cylinder was the same force seen by the load cell minus a small amount due to friction in the pin. The output from the tension load cell passed through the umbilicals to the Edgerton where it was monitored. Hydraulic hose ran from a hand operated pump on the Edgerton to the hydraulic cylinder so that the tension could be changed as desired. This was not a constant tension system. Stiction in the hydraulic cylinder kept the distance between the attachment points of the test cylinder a constant unless intentionally changed. Therefore tension varied slowly with current speed and mean drag force.

2.5 Test Cylinders

2.5.1 Cable

A 75 foot long instrumented cable was developed specifically for the experiments that were performed in the summer of 1981. The outer sheath for this cable was a single piece of clear flexible PVC tubing, which was 1 1/4 inches in outside diameter by 1.0 inch in inside diameter. Three 1/8 inch diameter stainless steel cables ran through the tubing and served as the tension carrying members. A cylindrical piece of 1/2 inch diameter neoprene rubber was used to keep the stainless steel cables spaced 120 degrees apart. The neoprene rubber spacer was continuous along the length except at seven positions where biaxial pairs of accelerometers were placed. Starting at the east end these positions were at L/8, L/6, L/4, 2L/5, L/2, 5L/8, and 3L/4. These accelerometers were used to measure the response of the cable. The accelerometers were Sundstrand Mini-Pal Model 2180 Servo Accelerometers which are sensitive to the direction of gravity. Each is 1/2 inch in diameter by 1.5 inches long. The biaxial pairing of these accelerometers made it possible to determine their orientation and hence extract real vertical and horizontal accelerations of the

cable at the seven locations. Three bundles of ten wires each ran along the sides of the neoprene spacer to provide power and signal connections to the accelerometers and to the drag measuring system. An Emerson and Cuming flexible epoxy was used to fill the voids in the cable and make it water tight. The weight per unit length of this composite cable was .7704 lbs/ft in air.

2.5.2 Steel Tubing

In a second set of experiments, the composite cable was placed inside a 1.631 inch O.D by 1.493 inch I.D. steel tube. The tubing was made of four equal length sections that were joined together. At the internal joints steel nipples were welded to each tube section and stainless steel threaded couplings were used to join them. The tubing was connected to the hydraulic cylinder and to the drag cell mechanism by custom made universal joints to provide pinned end conditions. These special end connectors also kept the cable inside the tubing under a slight tension, and neoprene spacers at intervals of 18 inches between the cable and tubing inhibited any relative motion betwwen the two. The remaining cavity was allowed to fill with water. The weight per unit length of the steel tubing with the cable inside and the voids flooded with water was 2.2344 lbs/ft., in air.

2.5.3 Lumped Masses

In another set of experiments, lumped masses were fastened to the bare cable and their effects studied. The lumped masses were PVC cylinders 12.0 inches long and 3.5 inches in diameter. A 1.25 inch hole was drilled through the center of each lump so that the cable could pass through. In addition, four .625 inch holes were drilled symmetrically around this 1.25 inch center hole so that copper tubes filled with lead could be inserted to change the mass of the lumps. In the field, it was difficult to force the cable through the holes drilled in the PVC so each mass was cut in half along the length of its axis. The masses were placed on the cable in halves and held together by hose clamps. Different tests

were run by varying the number and location of lumps and by changing the mass of the lumps. The results of these tests will not be reported on in this paper, but may be found in references (16) and (17).

2.5.4 <u>Faired Cable</u>

Finally, 11.6 x 1/16 inch diameter Endeco plastic stranded fairings were applied to the cable to evaluate their effectiveness as strumming suppression devices.

CHAPTER 3

DATA REDUCTION

3.1 Vector Rotation of Acceleration Time Histories

The orientation of the biaxial accelerometers is initially unknown. Because the cross-flow (vertical) and in-line (horizontal) vibration are of different character, it was useful to separate the measured acceleration into vertical and horizontal components. This required determining accelerometer orientation angle, which then permitted recovery of the vertical and horizontal components by vector rotation of the time histories. The accelerometers used were sensitive to gravity and gave a DC offset to the recorded signal. Fig 3 defines x'(t) and y'(t) as the actual orientation of the accelerometer axes. (θ is the angle of rotation necessary to describe the motion in the desired coordinate system. The x' and y' measurements have DC offsets (DCx and DCy) proportional to the component of gravity which was measured in that direction. From these DC offsets the angle θ may be obtained.

$$\theta = \tan^{-1}\left|\frac{DC_x}{DC_y}\right| + k\pi \qquad (3.1.1)$$

where K depends on the sign of DCx and DCy. After A has been found, the real vertical and horizontal accelerations x(t), y(t) can be found by the vector rotation:

$$X(t) = X'(t)\cos\theta - Y'(t)\sin\theta \qquad (3.1.2a)$$

$$Y(t) = X'(t)\sin\theta + Y'(t)\cos\theta \qquad (3.1.2b)$$

Figures 4 to 7 show sample acceleration time histories before and after rotation. Note that the real vertical acceleration has a DC offset equal to one g or 386.017 in/sec**2.

3.2 Integrator

In a continuous time description, Equation (3.2.1) represents the integration of acceleration a(t) tv get velocity v(t)
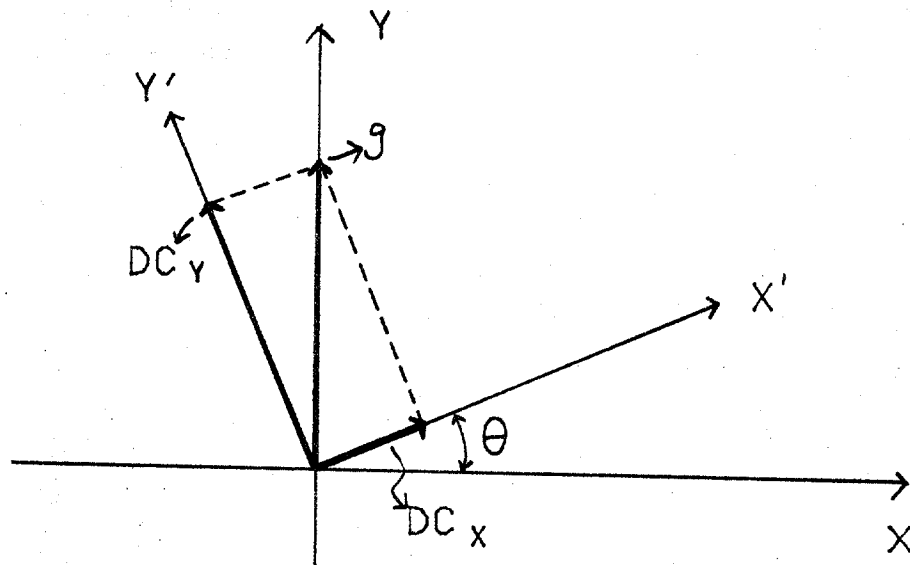
VECTOR ROTATION OF

RAW ACCELERATION

$$DC_X = g \, SIN$$

$$DC_Y = g \, COS$$

$$\Rightarrow \quad \theta = TAN^{-1}\left(\frac{DC_X}{DC_Y}\right)$$

$$X(t) = X'(t) \, COS\theta - Y'(t) \, SIN\theta$$

$$Y(t) = X'(t) \, SIN\theta + Y'(t) \, COS\theta$$

FIG. 3 RELATION BETWEEN ROTATED

ANGLE AND DC OFFSET
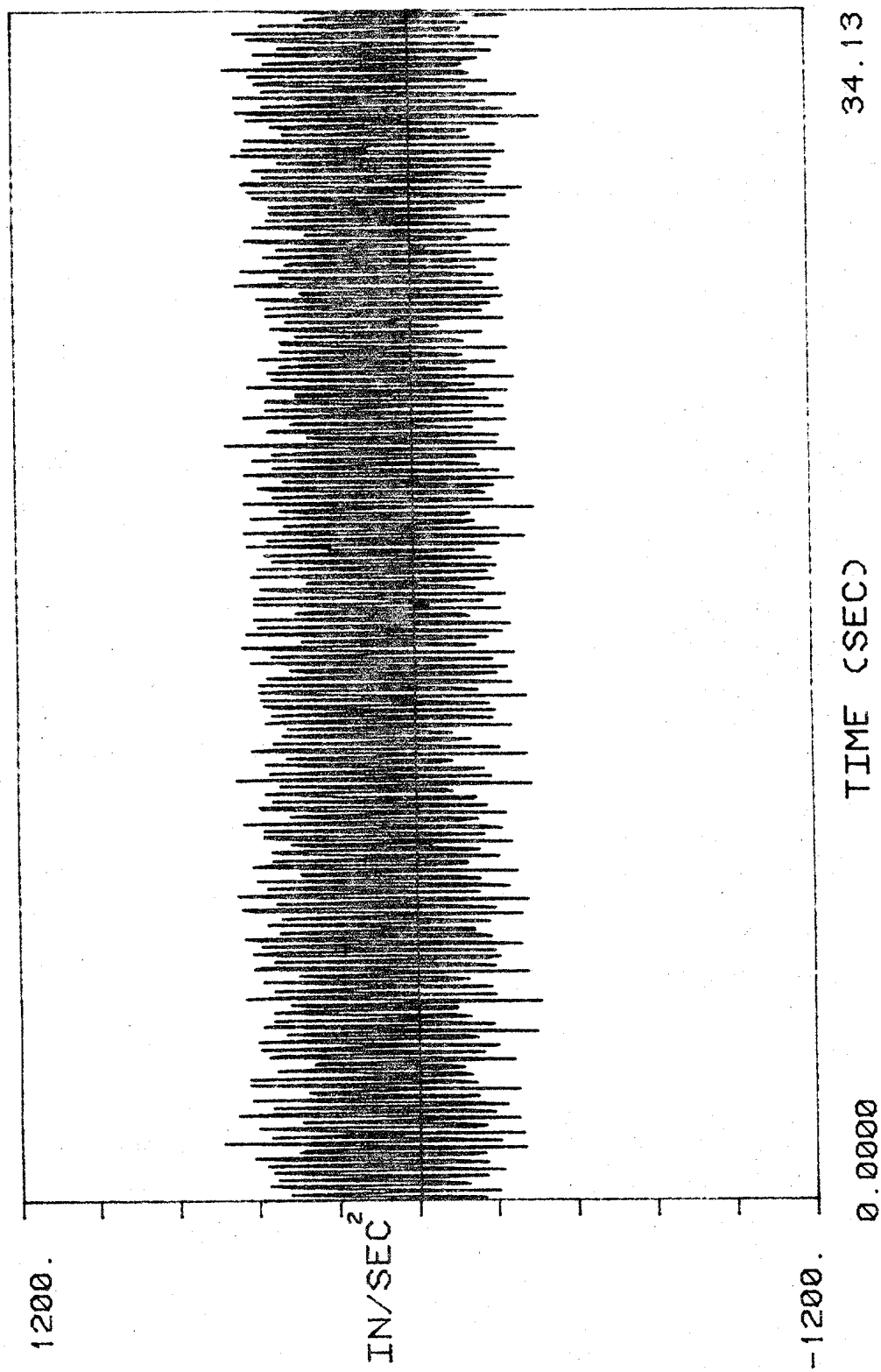
FIG. 4 RECORDED ACCELERATION BEFORE ROTATION

NEAR HORIZONTAL

12
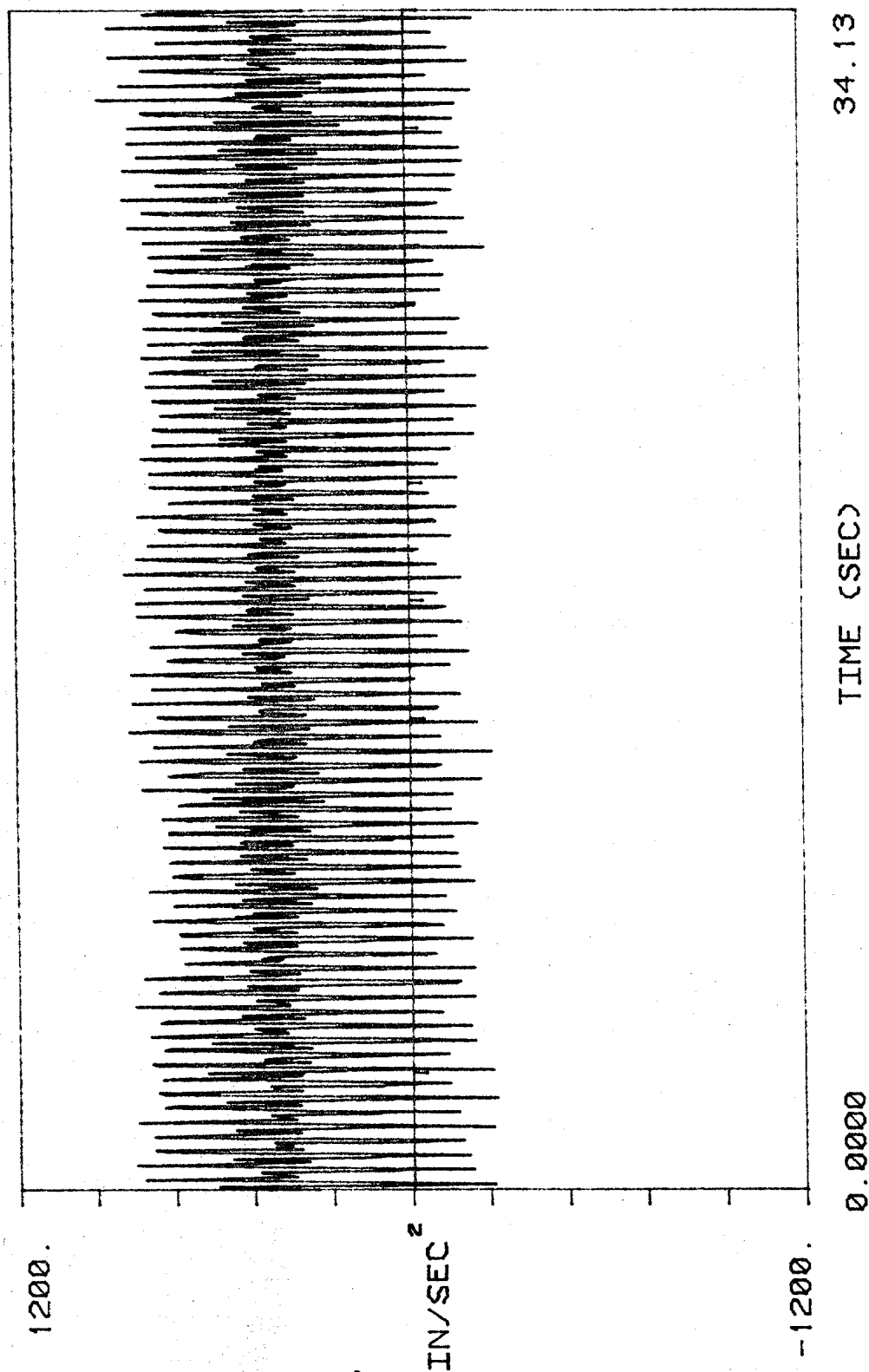
FIG. 5 RECORDED ACCELERATION BEFORE ROTATION

NEAR VERTICAL.

13
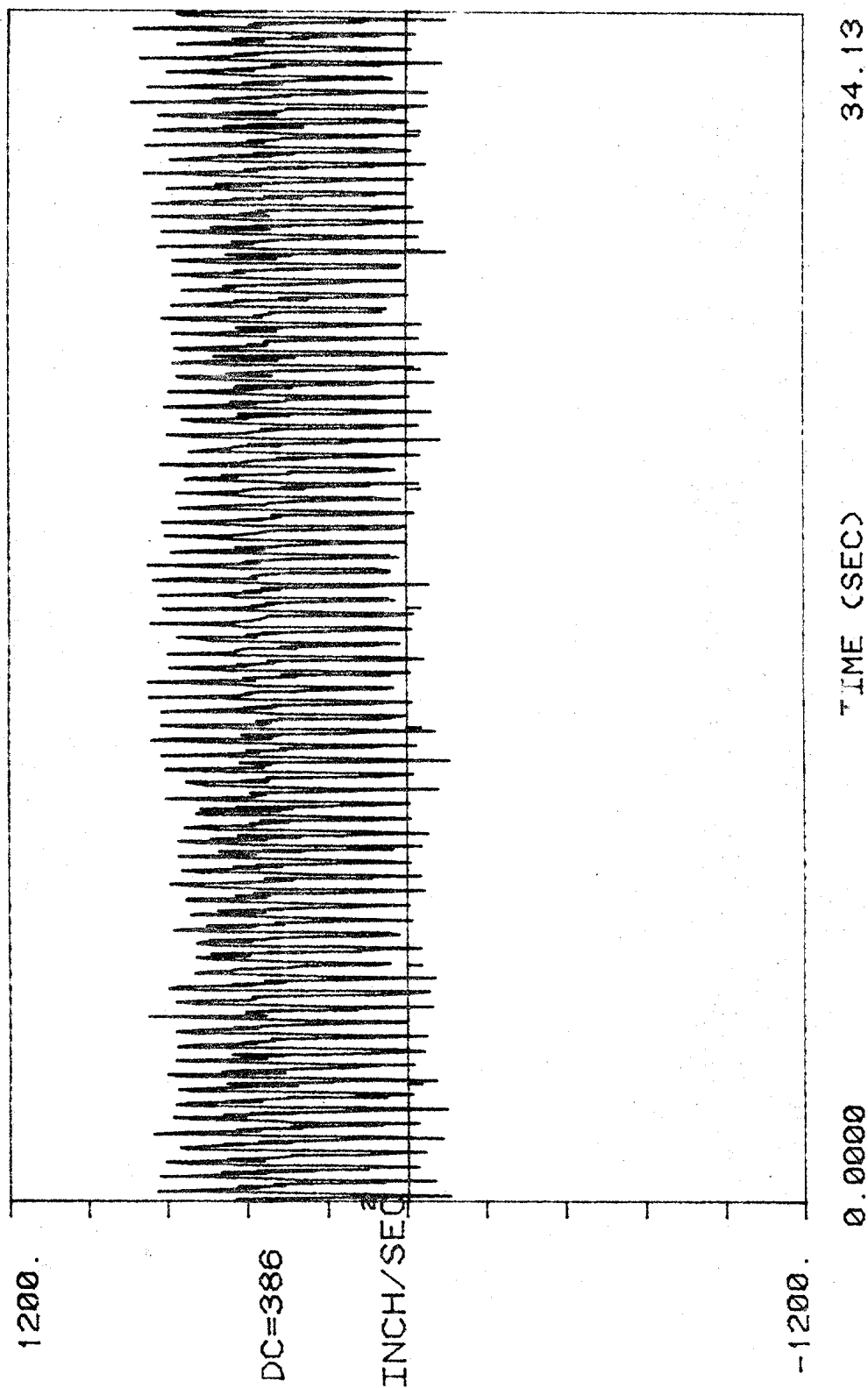
FIG. 6   REAL VERTICAL ACCELERATION

AFTER ROTATION OF 16.5 DEGREES

14
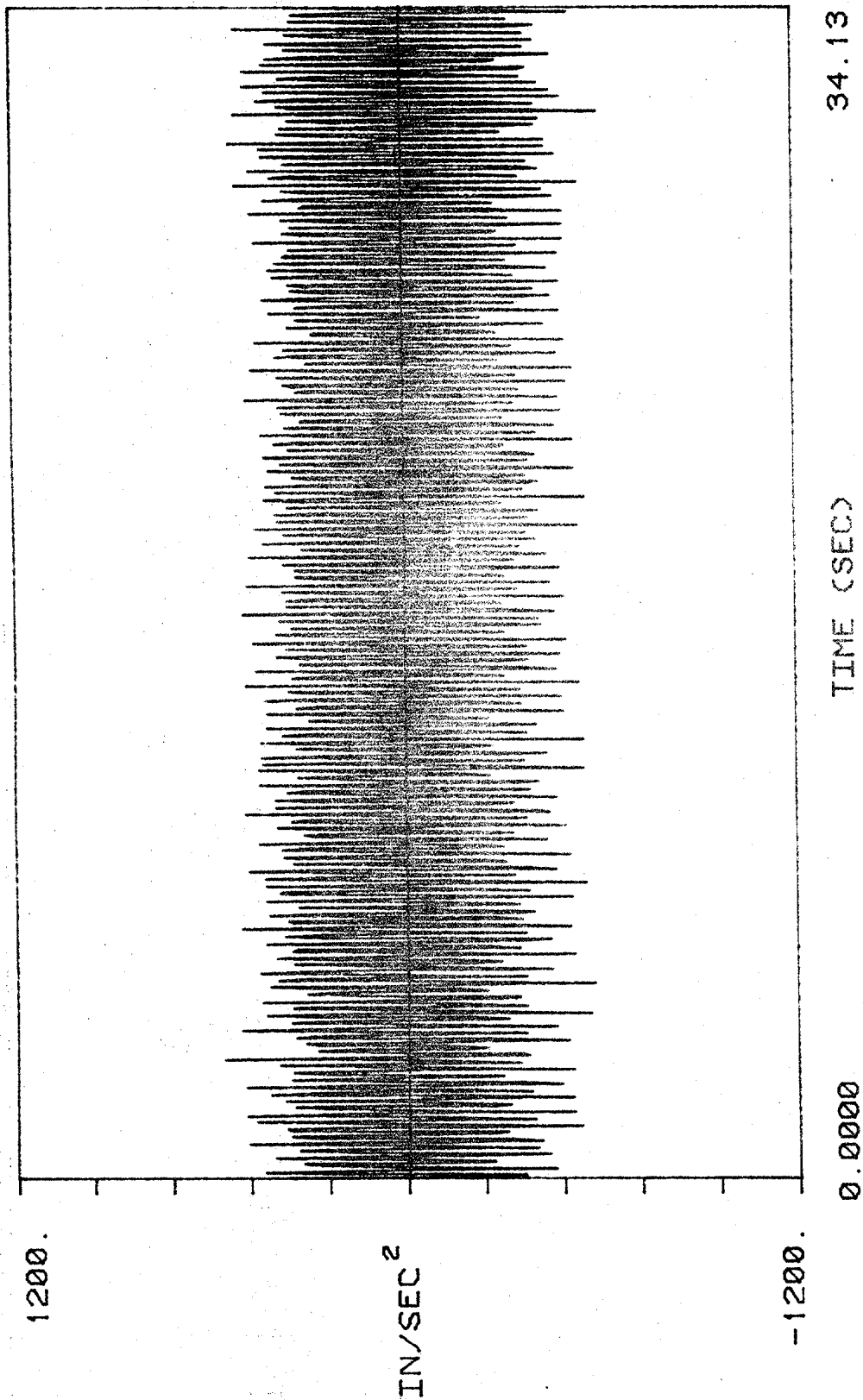
FIG. 7 REAL HORIZONTAL ACCELERATION
AFTER ROTATION OF 16.5 DEGREES

15
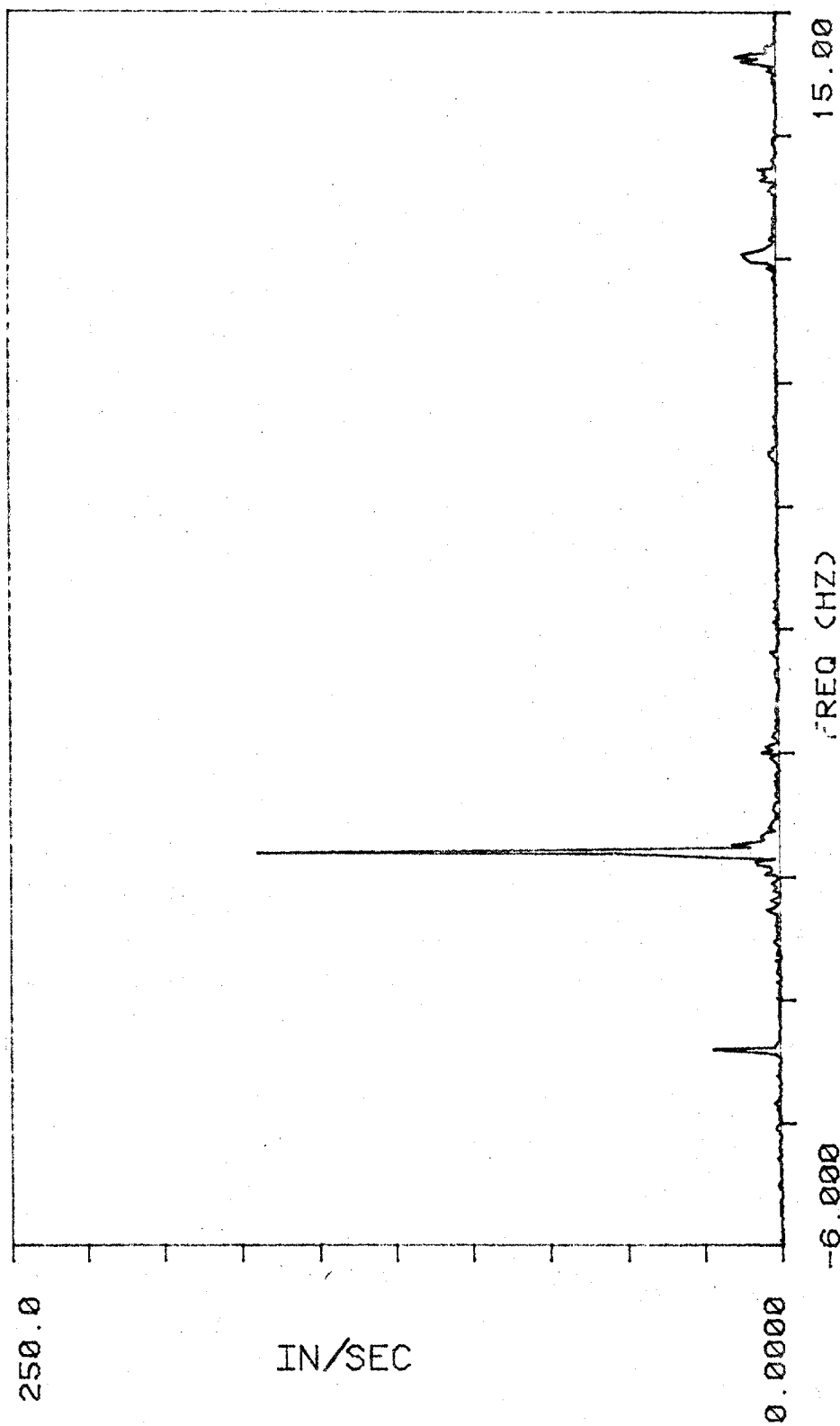
FIG. 8 FFT OF THE ACCELERATION AFTER ROTATION

(HORIZONTAL RESPONSE)

16

$$V(t) = \int_0^t a(t')dt' \tag{3.2.1}$$

A discrete time approximation for v(t) can be calculated by a linear constant coefficient difference equation.

$$V[n] = V[n-r]+T \sum_{k=0}^{m} b[k]a[n-k] \tag{3.2.2}$$

where r is the order of the filter and the b(k) are the filter coefficients, m is the degree of the filter, and T is the sampling period.

Generally, the properties of digital integrators have been developed in the time domain by fitting the data points with a smoothed curve. The time domain interpretation as presented in equation 3.2.2 has an equivalent frequency domain formulation. The Z-Transform of equation (3.2.2) leads to the system function H(z):

$$H(Z) = T \frac{\sum_{k=0}^{m} b(k)z^{-k}}{1-z^{-r}} \tag{3.2.3}$$

Evaluating H(z) on the unit circle of the z-plane yields the frequency response function H(w). If the numerator of H(z) is a mirror image polynomial then forward and backward integration in time will yield the same result. This leads to:

for m odd
$$H(w) = Te^{-i(\frac{m-r}{2})w} \frac{\sum_{k=0}^{[m/2]} b(k)\cos(\frac{m}{2} - k)w}{i \sin rw/2} \tag{3.2.3a}$$

for m even
$$H(w) = Te^{-i(\frac{m-r}{2})w} \frac{\frac{1}{2} b(\frac{m}{2}) + \sum_{k=0}^{m/2-1} b(k)\cos(\frac{m}{2} - k)w}{i \sin rw/2} \tag{3.2.3b}$$

The frequency response function for an ideal integrator is:

$$H_I(w) = \frac{T}{iw} \tag{3.2.4}$$

Recognizing that, if x(n) and X(w) are a Fourier transform

pair, then $x(n-m)$ and $\exp(-iwm)X(w)$ are also a Fourier transform pair. Any system function that can be written as:

$$H(iw) = |H(iw)| \, e^{ikw} \qquad (3.2.5)$$

where k is a constant, is a linear phase shift system. Let $x(n)$ be the input to $H(w)$ in equation 3.2.3 and $Hi(w)$ in equation 3.2.4 with $y(n)$ and $y'(n)$ being the respective outputs. Rewriting $H(w)$ and $Hi(w)$ as:

$$H(iw) = |H(iw)| \, \frac{e^{-i\frac{m-r}{2}w}}{i} \qquad (3.2.6)$$

$$H_I(iw) = |H_I(iw)| \, \frac{1}{i} \qquad (3.2.7)$$

Then the transfer function between $y(n)$ and $y'(n)$ is,

$$\frac{Y(iw)}{Y'(iw)} = \frac{|H(iw)|}{|H_I(iw)|} \, \exp\left(-i\frac{m-r}{2}w\right) \qquad (3.2.8)$$

There is a linear phase shift between the ideal integrator result and this integrator result. A comparision of the magnitudes of (3.2.3) and (3.2.4) can be used to examine the accuracy of the integrator. An error measurement $E(w)$ is defined as:

$$E(w) = 20 \, \log \left|\frac{H(w)}{H_I(w)}\right| = 20 \, \log \, w|H(w)| \qquad (3.2.9)$$

Fig. 9 shows $E(w)$ for a variety of integrators. For the Castine experiment, the sampling frequency was 30 Hz, and the typical frequency range for the cable response was from 2 to 7 Hz. This corresponds to dimensionless frequencies in the figure from 0.13 π to 0.47 π where π corresponds to half the sampling frequency. Fig. 9 shows that the error for Trapezoidal rule integration in this range is from 2% to 20%, and 0.1% to 5% for Simpson's rule. The errors are larger at the higher frequencies. Many maximally flat integrators have been presented in the literature (6). Fig. 9 shows two examples for filters of degree m=2 and 4. The error for m=4
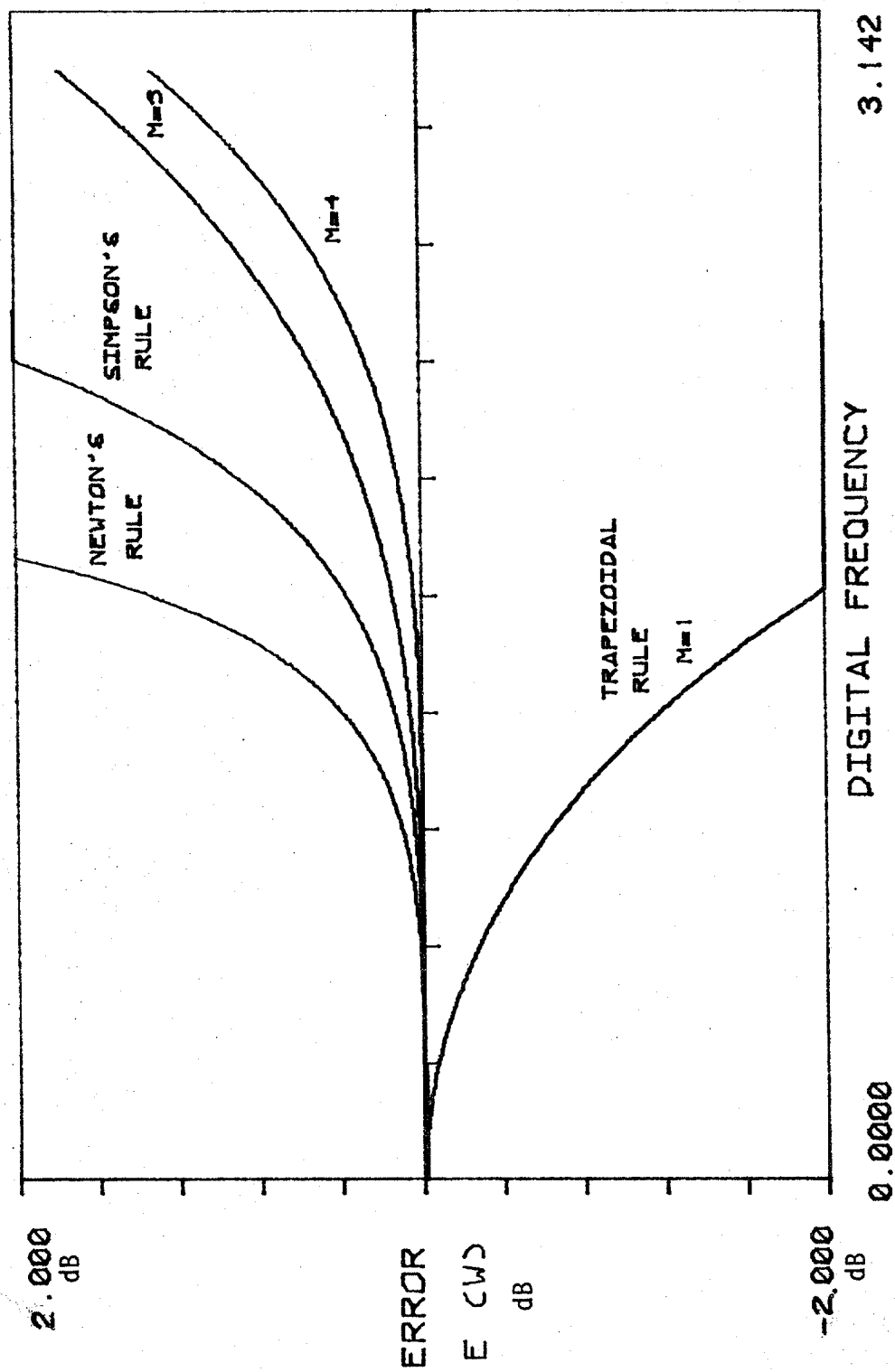
FIG. 9 ATTENUATION FOR DIFFERENT INTEGRATORS

is reduced to a maximum of 0.5% at the highest frequency of interest.

Schuessler and Ibler (13) pointed out two basic mistakes in the application of this integration formula. First, the filter coefficients b(k) should be time-varying instead of constant according to the equation:

$$b'(k,n) = \begin{array}{ll} b(k)\ u(n-r+k) & k=0,1,.,.,.,(r-1) \\ b(k) & k=r,r+1,.,.,m \end{array}$$

(3.2.10)

where b(k) are filter weights given in table 3.1 and 3.2 and u(k) is a unit step function. The reason is that according to the continuous integration equation (3.2.1) $v(0)=0$ must hold. But by using the digital integrator (3.2.2), $v(0)=b(0)a(0)$ rather than zero. If (3.2.9) is used, $v(0)=b'(0,0)a(0)=b(0)u(-r)a(0)=0$ which yields the correct result. Second, the Newton-Codes formulas are, in fact, valid only for $n=i*r$ with $i=0,1.^-$, so Schuessler and Ibler proposed that the sampling frequency at input and output should be different. This is accomplished by applying an interpolator to the input sequences before the integrator is applied. The combination of the interpolator and integrator into one system led them to propose a new integration formula.

$$V(n) = V(n-1) + \frac{T}{3} \sum_{k=0}^{2L-1} b'(k,n)\ a(n-k) \qquad (3.2.11)$$

where L is the length of the interpolator and

$$b'(n,k) = \left| \begin{array}{ll} b(k)\ u(n-L+k) & 0 \le k \le L-1 \\ b(k) & L \le k \le 2L-1 \end{array} \right.$$

(3.2.12)

the b(k) are the new filter coefficients given in table 3.3 This integrator was used in the analysis of the Castine data.

3.3 Low Frequency Noise Expansion

The cable velocity, v(t), and displacement, a(t), can be obtained from the acceleration, a(t), by numerical

integration. If v(0) is the initial velocity at t=0, the time of the start of data collection, then

$$v(t) = v(0) + \int_0^t a(t')dt' \qquad (3.3.1)$$

The initial velocity $v(0)$ is unknown. However, a bounded displacement d(t) is desired. This requires that there be no linear trend or DC component in the velocity $v(t)$ The value v(0) can be arbitrarily set to zero. Following the integration of a(t) a atraight line is fitted to $v(t)$ The offset and trends which are found may be then removed from $v(t)$ Equation 3.3.1 can be rewritten as:

$$v(t) = a(t) * u(t) \qquad (3.3.2)$$

where u(t) is the unit step function and * denotes a convolution integral. Taking the Fourier transform of Equation 3.3.2 yields:

$$V(w) = A(w)[\pi\delta(w) + \frac{1}{iw}] = A(0)\pi + \frac{A(w)}{iw} \qquad (3.3.3)$$

$$A(0) = \int_{-\infty}^{\infty} a(t)dt \qquad (3.3.4)$$

The term A(0) can be removed by fitting a straight line to a(t) to remove any linear trend or DC component in acceleration a(t). The transfer function between a(t) and v(t) is:

$$H(w) = \frac{V(w)}{A(w)} = \frac{1}{iw} \qquad (3.3.5)$$

The same procedure can be applied to integrate v(t) to get d(t) except that the assumption for the zero mean d(t) is no longer true. But, we are interested only in the dynamic response of the cable, so d(0) can be set arbitrarily. Integration has the characteristics of a low-pass filter with a gain which goes to infinity as the frequency goes to zero. This leads to the undesirable expansion of low frequency noise in the integration process. Fig. 7 shows a sample of
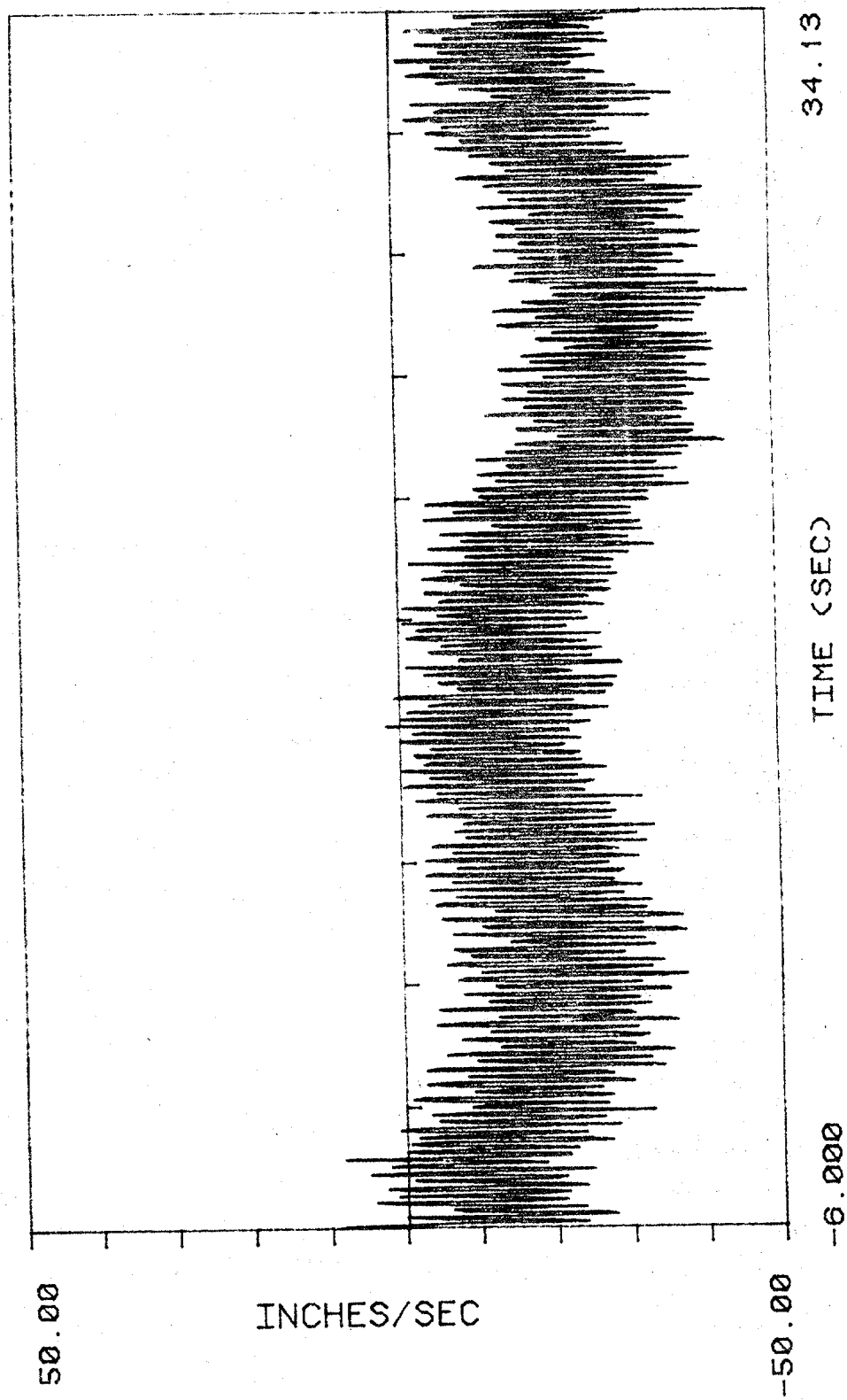
21

FIG.10 VELOCITY AFTER ONE INTEGRATION WITH
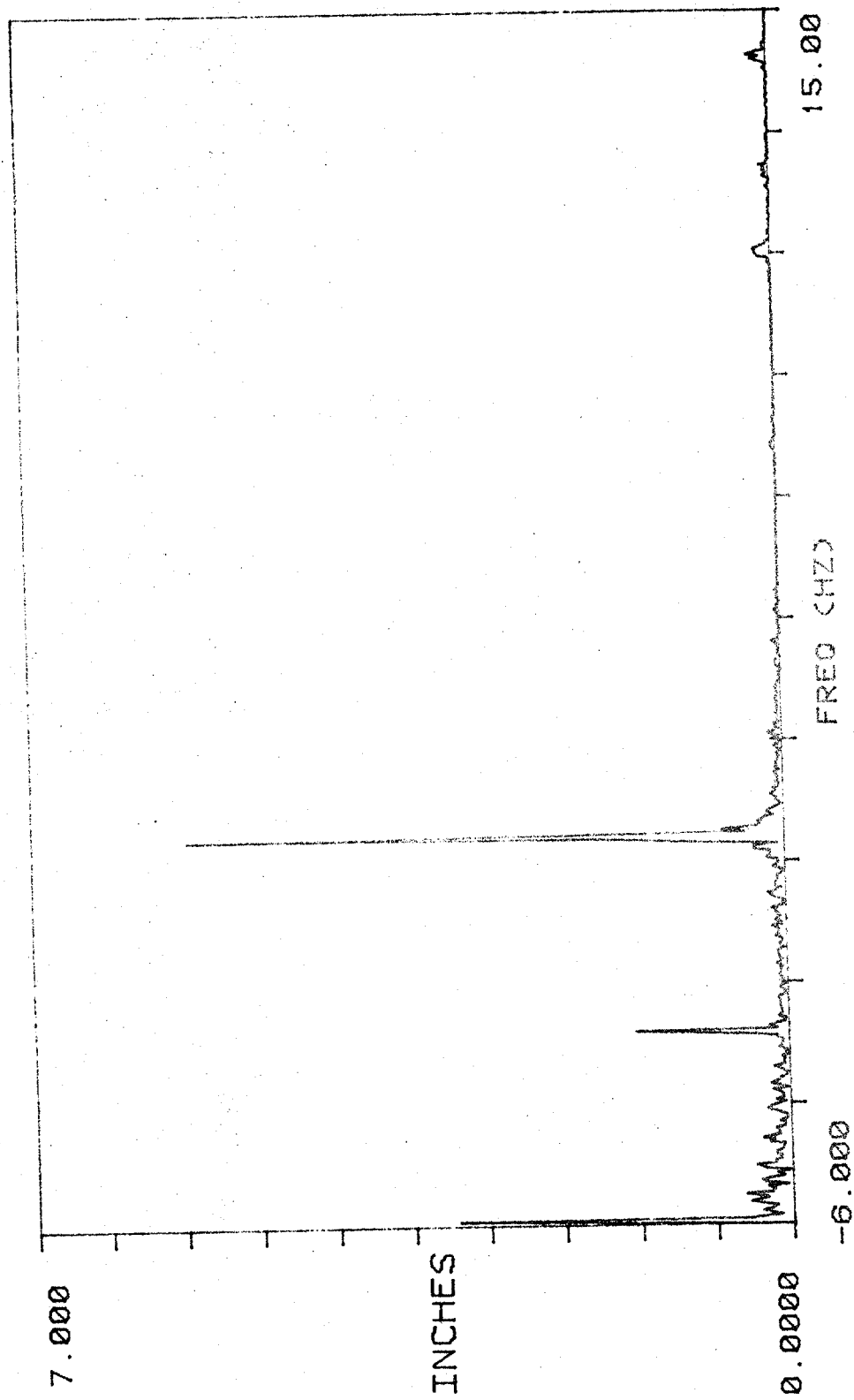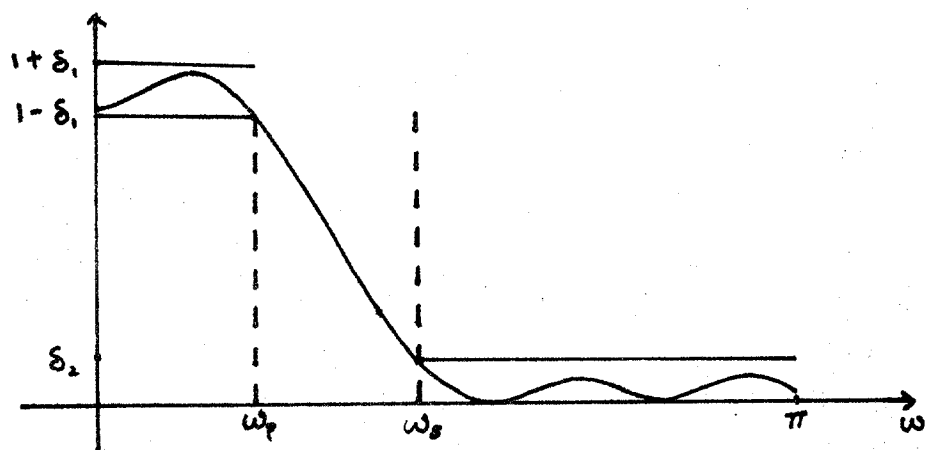LOW-FREQUENCY NOISE EXPANSION

FIG.11 FFT OF THE VELOCITY IN FIG.10

FIG.12 FILTER SPECIFICATION
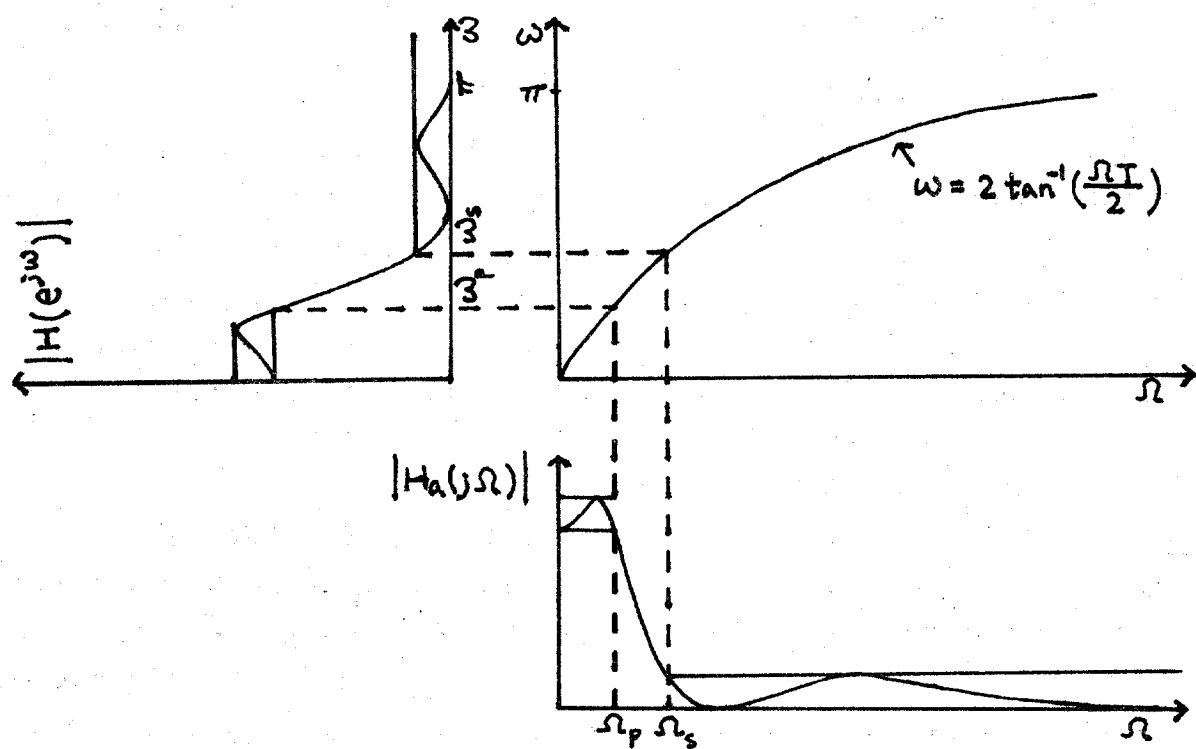

$\omega = 2\tan^{-1}\left(\frac{\Omega T}{2}\right)$

FIG.13   ANALOG-DIGITAL BILINEAR
TRANSFORMATION

an acceleration time history. Fig. 8 is the FFT of this acceleration. A negligible component of low frequency noise is shown. Figures 10 and 11 show that after integration, low frequency noise dominates the velocity signal.

This reveals that low frequency noise expansion leads to unacceptable integration errors. To correct the problem, a high-pass filter is required.

3.4 High-Pass Filter

A digital filter is a linear time-shift-invariant system represented by a linear constant coefficient difference equation (LCCDE):

$$y[n] = \sum_{k=1}^{N} a_k \, y[n-k] + \sum_{k=0}^{M} b_k \, x[n-k] \tag{3.4.1}$$

The corresponding system function is given by

$$H(Z) = \frac{\sum_{k=0}^{M} b_k \, z^{-k}}{1 - \sum_{k=1}^{N} a_k z^{-k}} \tag{3.4.2}$$

where x(n) is the input signal, y(n) is the output signal, and ak and bk are filter coefficients. For a stable causal filter all the poles of this system function must lie inside the unit circle. There are three basic steps in the design of a digital filter: (1) The specification of the desired filter properties; (2) the determination of the transfer function possessing those properties and (3) the implementation of the filter.

For an ideal low-pass (or high-pass) filter, the transfer function magnitude contains a sharp discontinuity at the cut-off frequencies and the required filter order is infinite. Thus a transition band at the cut-off frequencies and a tolerance error in pass-band and stop-band are provided to approximate the desired filter. In step (1), the filter specification must include these tolerance magnitudes and the transition bandwidth. Fig. 12 shows these specifications for a low-pass filter.

If the system function H(z) in (3.4.2) contains poles

solely at the origin, the filter is called a finite impulse response (FIR) filter. Otherwise it is an infinite impulse response (IIR) filter.

A FIR filter is always stable and a linear phase is always achievable by choosing a symmetric impulse response function h(n). For the same desired filter characteristics, the FIR filter must be of a much higher order than the comparable IIR filter, and therefore the FIR filter may require excessive computer time.

The design of an IIR filter involves the transformation of an analog filter into a digital filter. There are several analog low-pass filters available, including the Butterworth, Chebyshev, and elliptic filters. By using the proper transformation between the analog and digital systems, an analog low-pass filter can be designed for which the corresponding digital filter meets the desired specification.

There are two requirements for the transformation of an analog system into a digital system. First, the imaginary axis of the s-plane must map onto the unit circle of the z-plane. This means that the properties of the frequency response function have been preserved. The second requirement is that a stable analog filter must be transformed into a stable digital filter, i.e. all the poles in the left half s-plane must map into the inside of the unit circle in the z-plane.

The Bilinear transformation (10) for mapping between the s-plane and the z-plane is given as:

$$S = \frac{2}{T} \frac{1-z^{-1}}{1+z^{+1}} \tag{3.4.3}$$

The unit circle in the z-plane is mapped according to:

$$S = \frac{2}{T} \frac{1-e^{-jw}}{1+e^{-jw}} = \frac{2}{T} \tan \frac{w}{2} = \sigma + i\Omega \rightarrow \Omega = \frac{2}{T} \tan \frac{w}{2} \tag{3.4.4}$$

Thus, the unit circle is mapped onto the imaginary axis of

the s-plane. Also, the left half of the s-plane is mapped
into the inside of the unit circle of the z-plane. Fig. 13
demonstrates the transformation. The procedure to design an
IIR low-pass filter involves the following four steps:

(1): Specifying the desired filter properties.

(2): Mapping those specifications into an analog filter using
the Bilinear transformation.

(3): Choosing an analog filter and determining those
parameters which meet the analog filter specification
requirements.

(4): Mapping the analog filter to a digital filter using the
bilinear transformation.

A high-pass filter can be designed by applying an
appropriate frequency transformation from a low-pass filter.
Let H(zl) and H(z) be the desired system functions of the
high-pass filter and corresponding low-pass filter. One
method of transformation is by using the following relation:

$$z^{-1} = -\frac{\alpha + z_1^{-1}}{1 + \alpha z_1^{-1}}$$
(3.4.5)

Fig. 14 shows the relation between H(wl) and H(w) The
design procedure for a high-pass filter involves the
following steps:

( ): Specification of the desired high-pass filter H(wl)

(^): Transformation to the equivalent low-pass filter H(w)
using equation (3.4.5)

(3): Application of the steps for the design of a low-pass
filter H(w)

(4): Transformation to the high-pass filter H(wl) by using
equation (^.4.5)

An IIR elliptic high-pass filter of the smallest
possible order is used to prevent low frequency noise
expansion in the double integration procedure. A computer
program for the design of an IIR elliptic filter has been
published by Gray and Markel (5). The input data to this
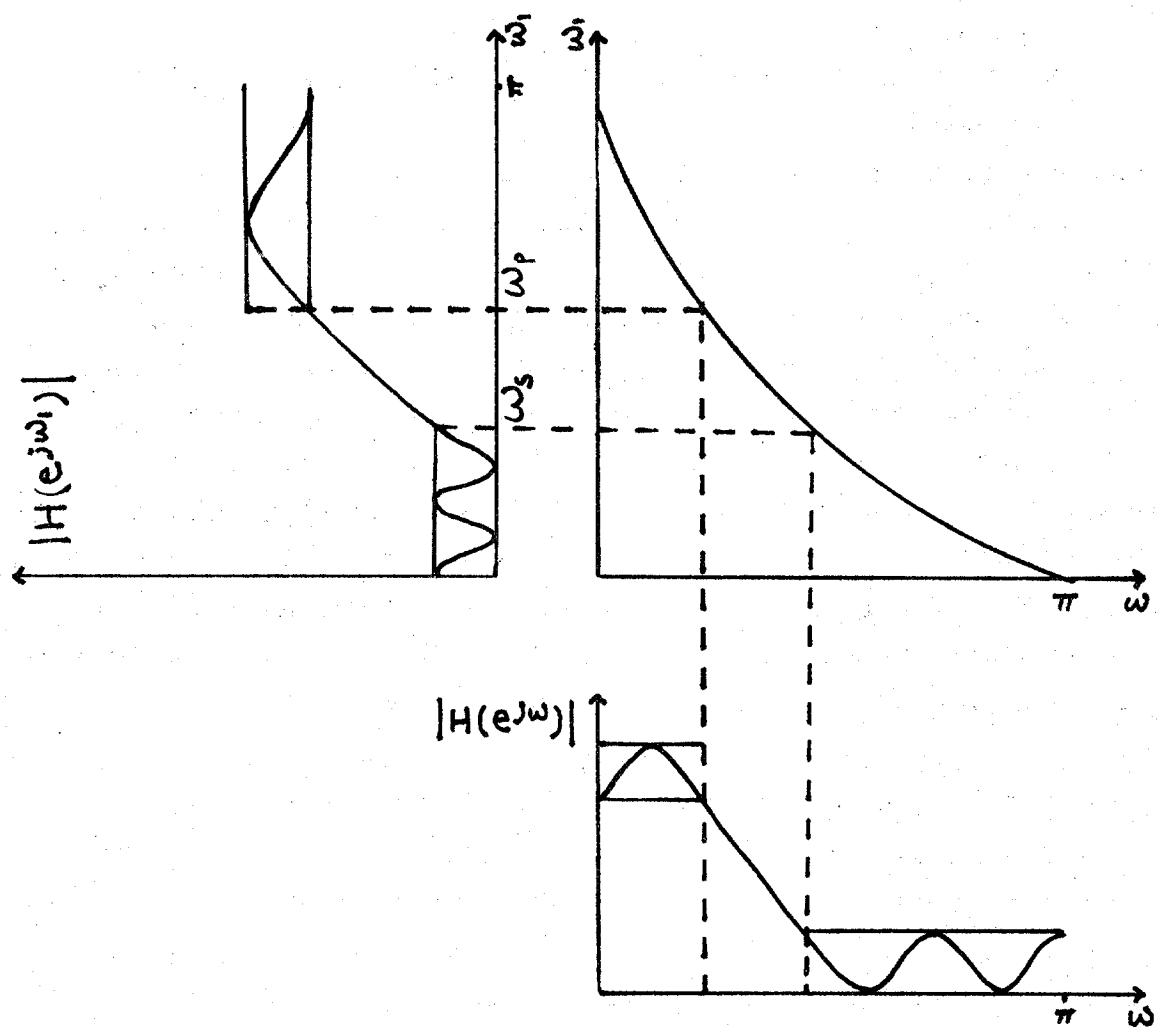program includes the tolerance error in pass-band and

27

FIG.14 TRANSFORMATION FROM LOW-PASS
TO HIGH-PASS

stop-band, the stop-band and pass-band edge frequencies and
the filter order N which may be estimated from design charts
(10). The output gives the position of zeros and poles for
the desired filter system function H(z).

A cascade form of implementation is used by writing H(z)
as a product of second-order factors as:

$$H(Z) = \prod_{k=1}^{N/2} (a_{0k} + a_{1k}Z^{-1} + a_{2k}Z-2) \qquad (3.4.6)$$

This separates the whole system into a series of several
second-order systems. The output of one system becomes the
input of the next. In general, this form of implementation
is less sensitive to the parameter quantization effect.

An IIR recursive filter always has nonlinear phase
characteristics. For this research, accurate phase
information is required in order to conduct the modal
analysis. The following steps ('') were used to eliminate
the nonlinear phase effects. Let x(n) and y(n) be the
sequences before and after the filter respectively. R is the
time reverse device, and H(z) is the filter system function.
These can be used in the following sequence

$$x[n] \longrightarrow [H(Z)] \overset{r[n]}{\longrightarrow} [R] \overset{S[n]}{\longrightarrow} [H(Z)] \overset{t[n]}{\longrightarrow} [R] \longrightarrow y[n]$$

$$R(w) = X(w) \ H(w)$$
$$S(w) = R(-w)$$
$$T(w) = S(w) \ H(w)$$
$$Y(w) = T(-w) \qquad (3.4.7)$$

Those relations imply the following:

$$Y(w) = X(w) H(w) H(-w) = X(w) |H(w)|^2 \qquad (3.4.8)$$

The new system function between x(n) and y(n) is the square
of the magnitude of the original filter's system function and
has zero phase shift.

3.5 Double Integration Procedures

A summary of the procedure for double integrating a
digital acceleration signal follows. The procedure contains

29

the following eleven steps:

Step 1. Determine the rotation angle of the accelerometers and use them to obtain the real vertical and horizontal accelerations.

Step 2. Using the method of least squares, fit a straight line to the block of data to be integrated. Use this to remove DC offsets and trends from the data prior to integration. The block length is 1024 data points in the results presented here.

Step 3. Obtain the acceleration spectrum and divide it by $1/w^{**}4$ to obtain the theoretical displacement spectrum. Use these two spectra as a subjective aid in the determination of the high-pass cutoff frequency necessary for the prevention of low-frequency noise expansion.

Step 4. High-pass filter the acceleration signal using an IIR elliptic filter to remove any low frequency noise.

Step 5. Integrate the acceleration signal using the Schuessler-Ibler integrator to obtain velocity.

Step 6. Least square fit a straight line to the velocity time history to remove the DC offset and linear trend.

Step 7. High-pass filter the velocity signal using the IIR elliptic filter to remove low-frequency components that were expanded in Step 5.

Step 8. Integrate the velocity signal using the Schuessler-Ibler integrator to obtain displacement.

Step 9. Least squares fit a straight line to the displacement time history to remove offsets and linear trend.

Step 10. High-pass filter the displacement signal using the IIR elliptic filter to remove low-frequency components that were expanded in Step 8.

Step 11. Plot summary data such as root-mean-squares, spectra, time series and two dimensional cylinder

motion time series.

CHAPTER 4
RESPONSE OF CYLINDERS

In the preceeding chapter, the data analysis process was presented, including vector rotation, filter design, and double integration procedures. In this chapter, typical analysis results of cylinder motions at lock-in and non-lock-in are presented. Compressed 2 1/2-hour records of drag coefficient, current speed, and RMS displacement response are also presented.

4.1 Cylinder Motion at Lock-in

Lock-in occurs when the vortex shedding frequency falls within a few percent of a natural frequency of the cylinder. The vortex shedding process is synchronized with the cylinder's motion, and a stable sinuisoidal transverse displacememt of nearly constant amplitude is observed. Fig. 15 shows an example of cross flow displacement of the pipe at L/4 during lock-in with the third mode. Fig. 16 is the corresponding FFT. A single dominant peak is observed. A narrow-band lift force is associated with this response.

In the horizontal direction, the motion is quite different from the vertical response at lock-in. A periodic but nonsinusoidal displacement is observed in the horizontal direction as shown in Fig. 17. Fig. 18 presents the magnitude of the FFT. The dominant frequency in horizontal direction is exactly double that in the vertical direction. The reason for this is that during the shedding of two vortices, one from each side off the cylinder, the lift force completes one cycle, but in the horizontal direction the drag force variation completes two cycles, one for each vortex shed. The result is that the dominant horizontal response frequency is exactly twice that of the vertical. The FFT in Fig. 18 reveals that the horizontal vibration also includes a small response component at the cross-flow vibration response frequency. This secondary frequency component accounts for the beat phenomena in Fig. 17. At lock-in the vertical and
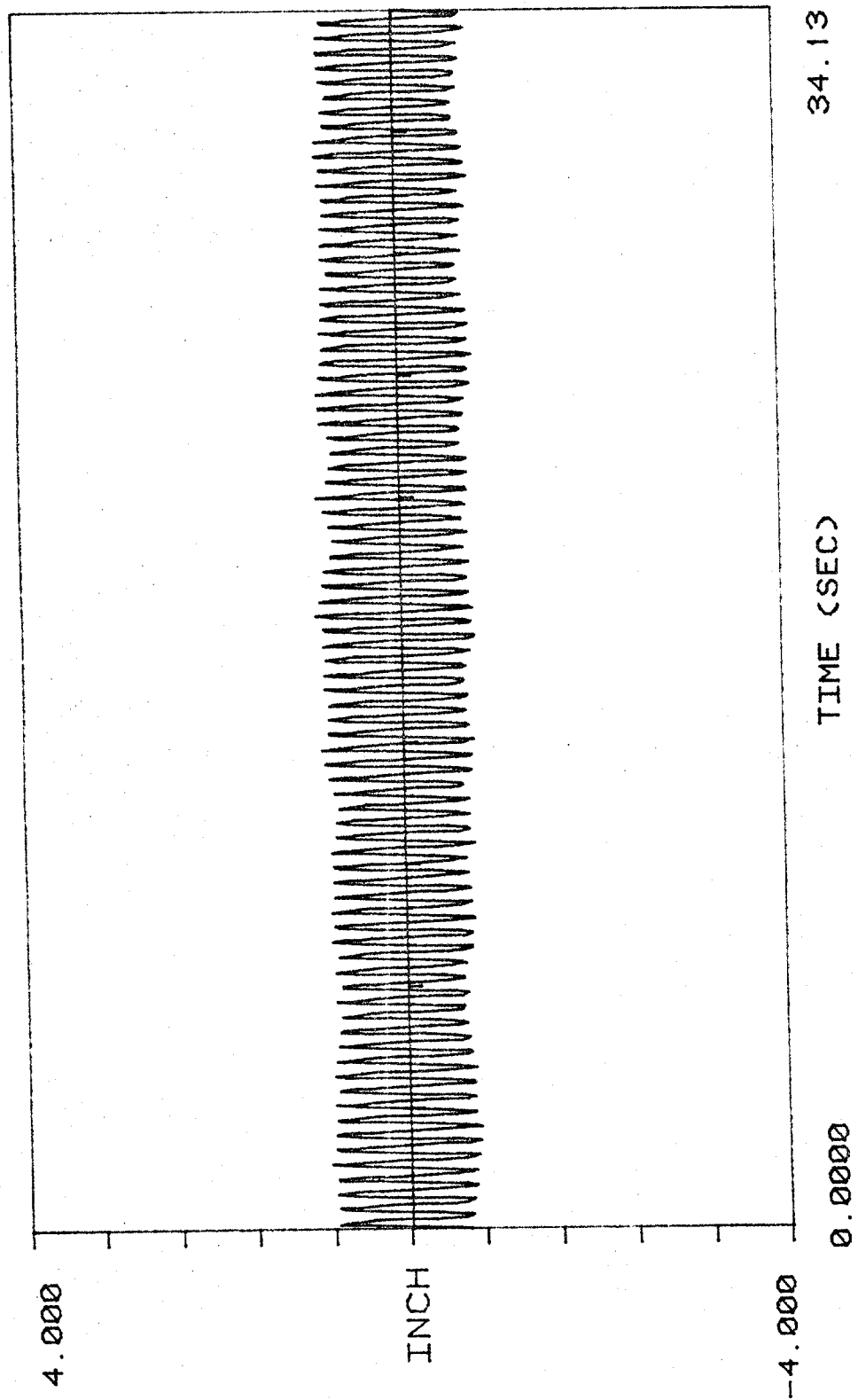
FIG.15 VERTICAL DISPLACEMENT OF
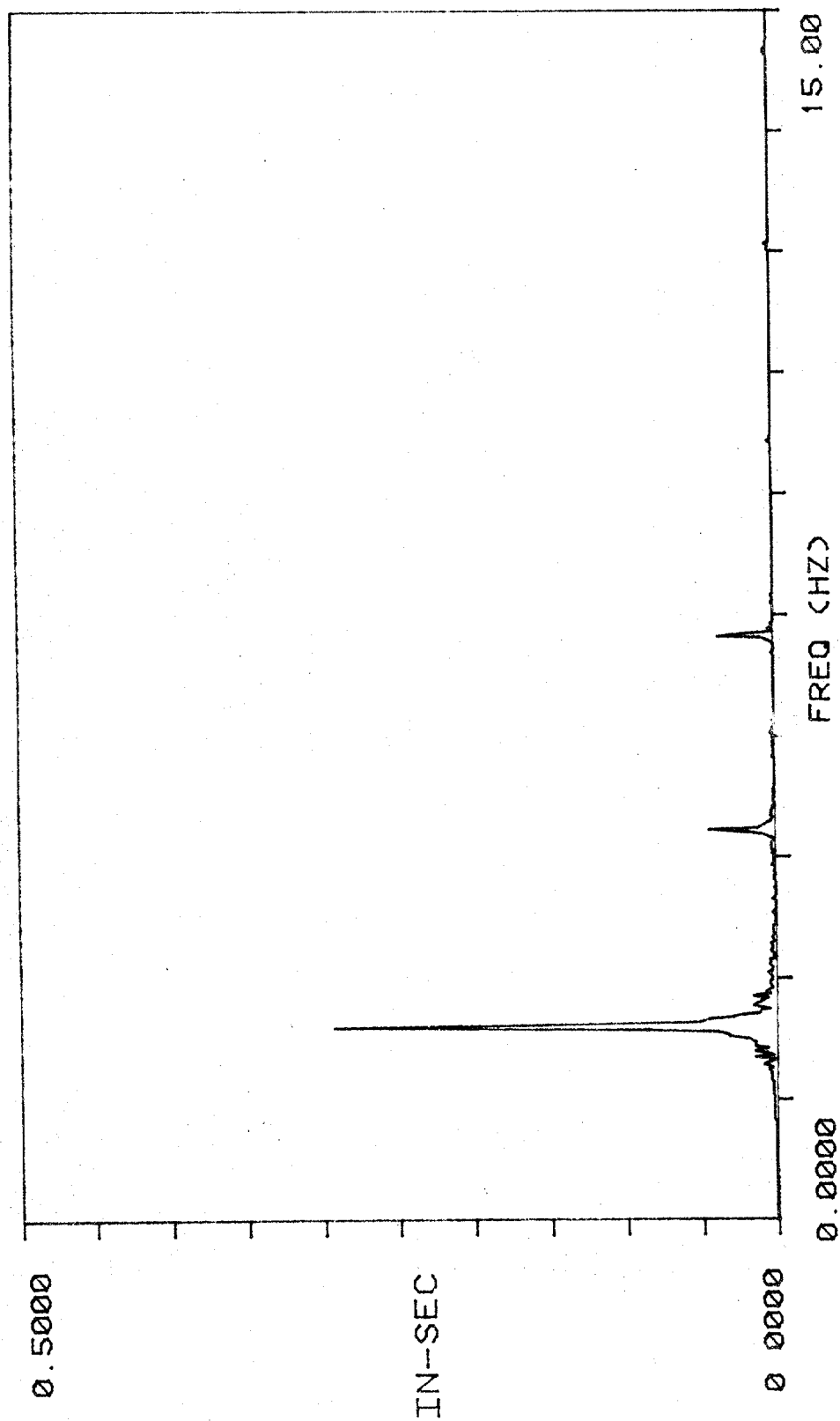THE PIPE AT LOCK-IN AT L/4

33

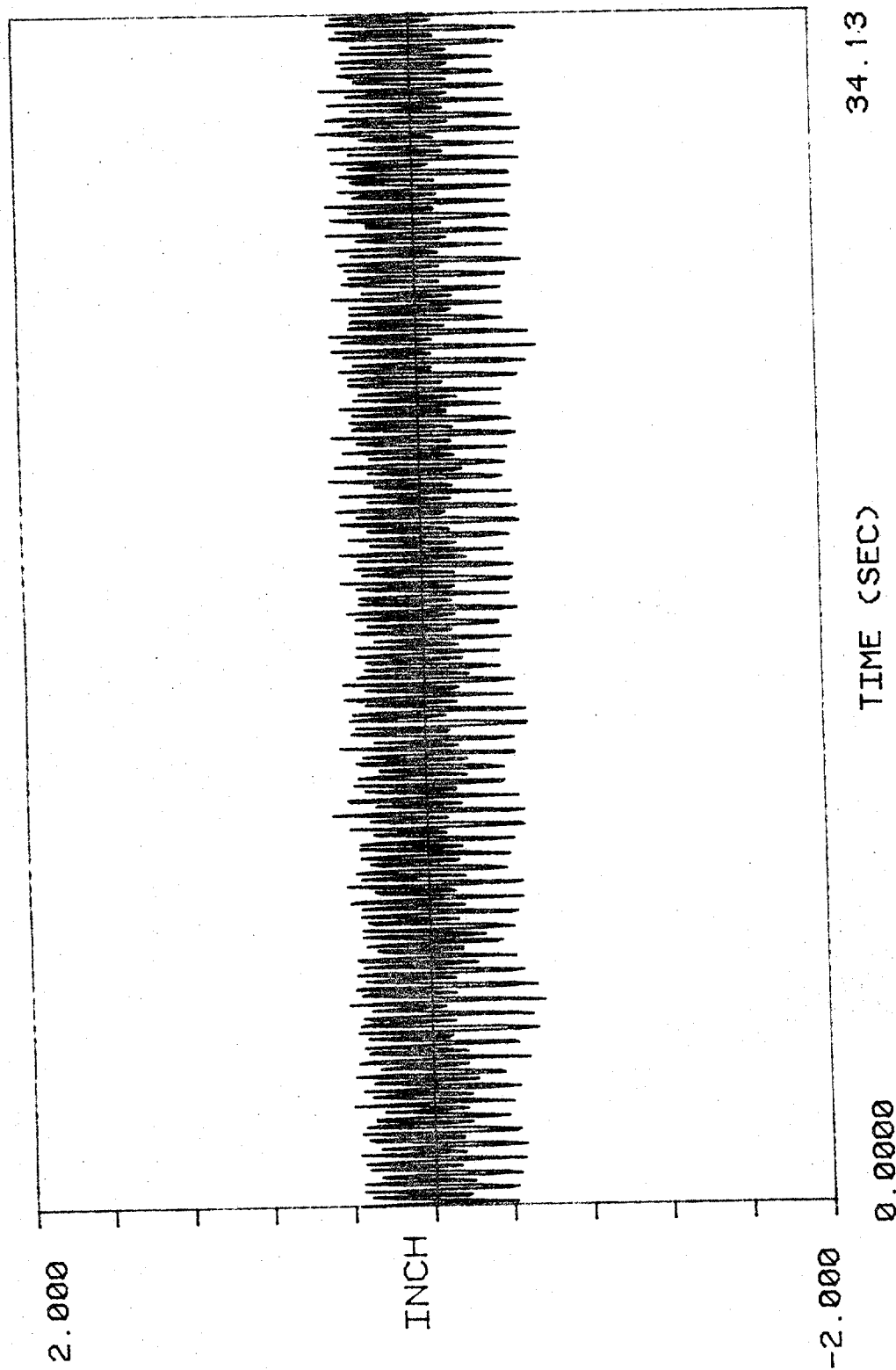FIG. 16   FFT OF THE DISPLACEMENT IN FIG.15

34

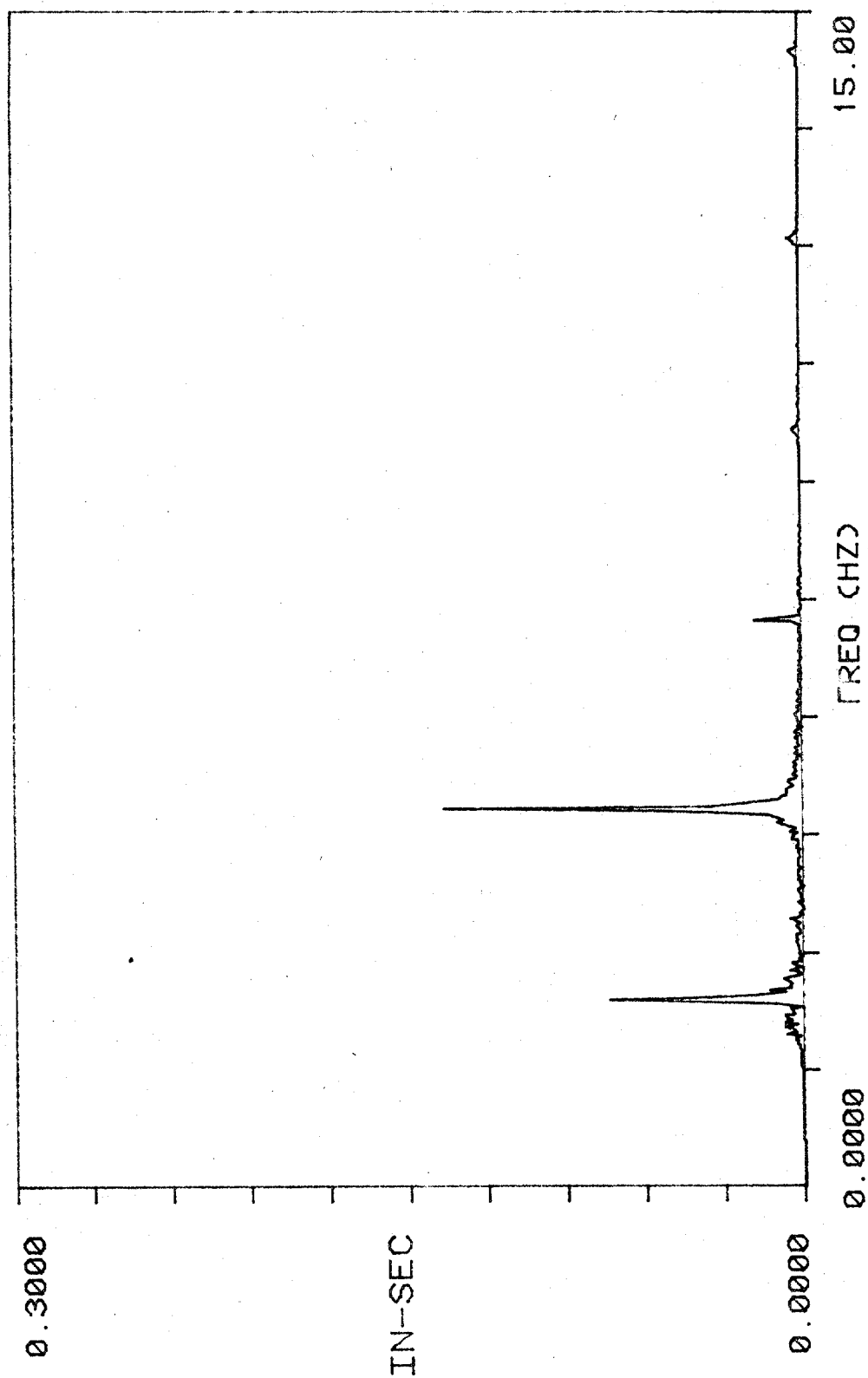FIG.17 HORIZONTAL DISPLACEMENT OF
THE PIPE AT LOCK-IN AT L/4
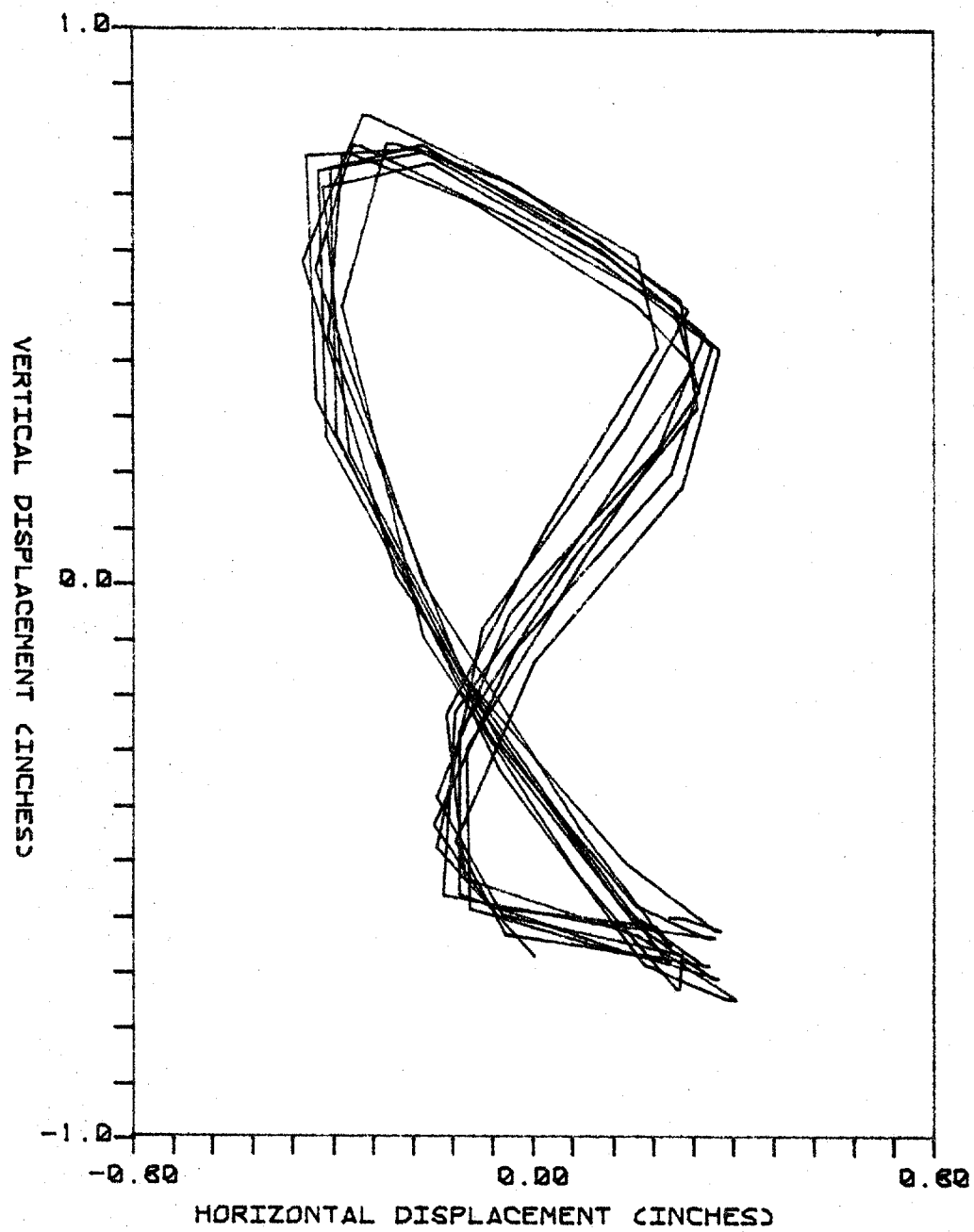
FIG.18 FFT OF THE DISPLACEMENT IN FIG.17

36

FIG.19 TWO-DIMENSIONAL MOTION TIME
HISTORY AT LOCK-IN AT L/4

horizontal excitations and responses are highly correlated. By double integration of both horizontal and vertical accelerations to obtain displacement time histories, it is possible to plot the trajectory of the motion of a point on the cylinder. Fig. 19 shows the motion at L/4 projected on to a plane which is normal to the cylinder axis. In this case the vertical motion was lock-in at third-mode and the horizontal motion was at twice the frequency of the vertical motion and was dominated by response in the fifth-mode. A small amount of third-mode motion also appears in the horizontal response. Without it there would be nearly perfect figures of eight.

At this point in the analysis, one does not generally know for certain which natural modes of vibration are responding. It will in fact be shown that the horizontal response which results from cross-flow lock-in does not always excite a resonant natural frequency. Mode shape identification is required to isolate individual contributing vibration modes. This is discussed in Chapter 5.

4.2 Cylinder Motion at Non-lock-in

When the vortex shedding frequency is outside of the lock-in range, non-lock-in vibration results. The response is characterized by fluctuations of amplitude and frequency in both vertical and horizontal directions. The lift force correlation length along the cylinder becomes much shorter than that at lock-in. Figs. 20 through 23 show typical displacement time histories and their FFTs in the cross-flow and in-line directions at L/8. Wide band lift and drag forces are implied. Figure 24 shows the corresponding displacement trajectories at L/8. For the data presented in Figs. 20 and 22, the response is due to many different modes. As will be shown in Chapter 5, the horizontal response peaks in Fig. 23 are due to the fourth, fifth, sixth and seventh modes.

4.3 Current, Drag Coefficient and RMS Displacement

The RMS data for in-line and transverse displacements
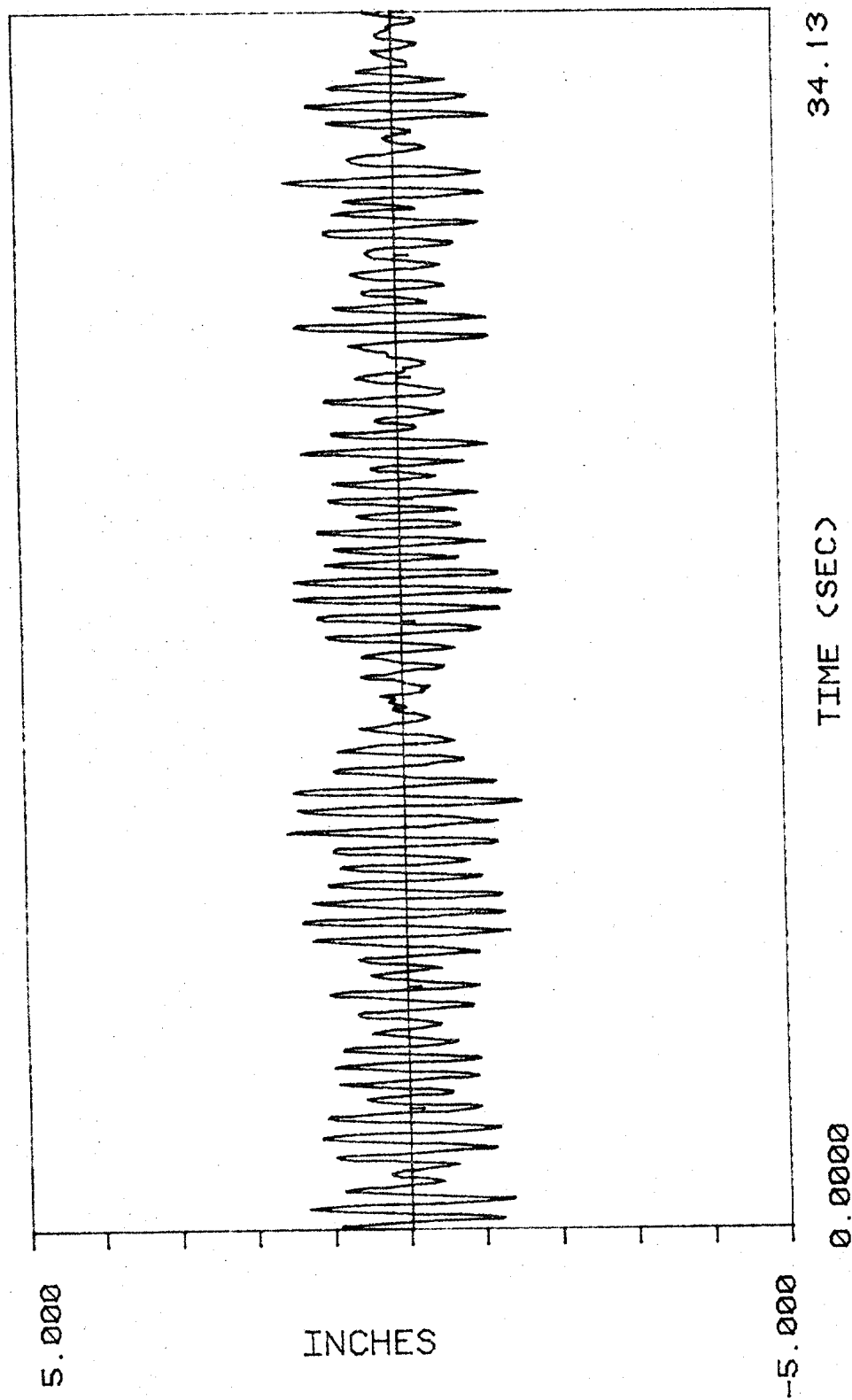
38

FIG. 20 VERTICAL DISPLACEMENT OF
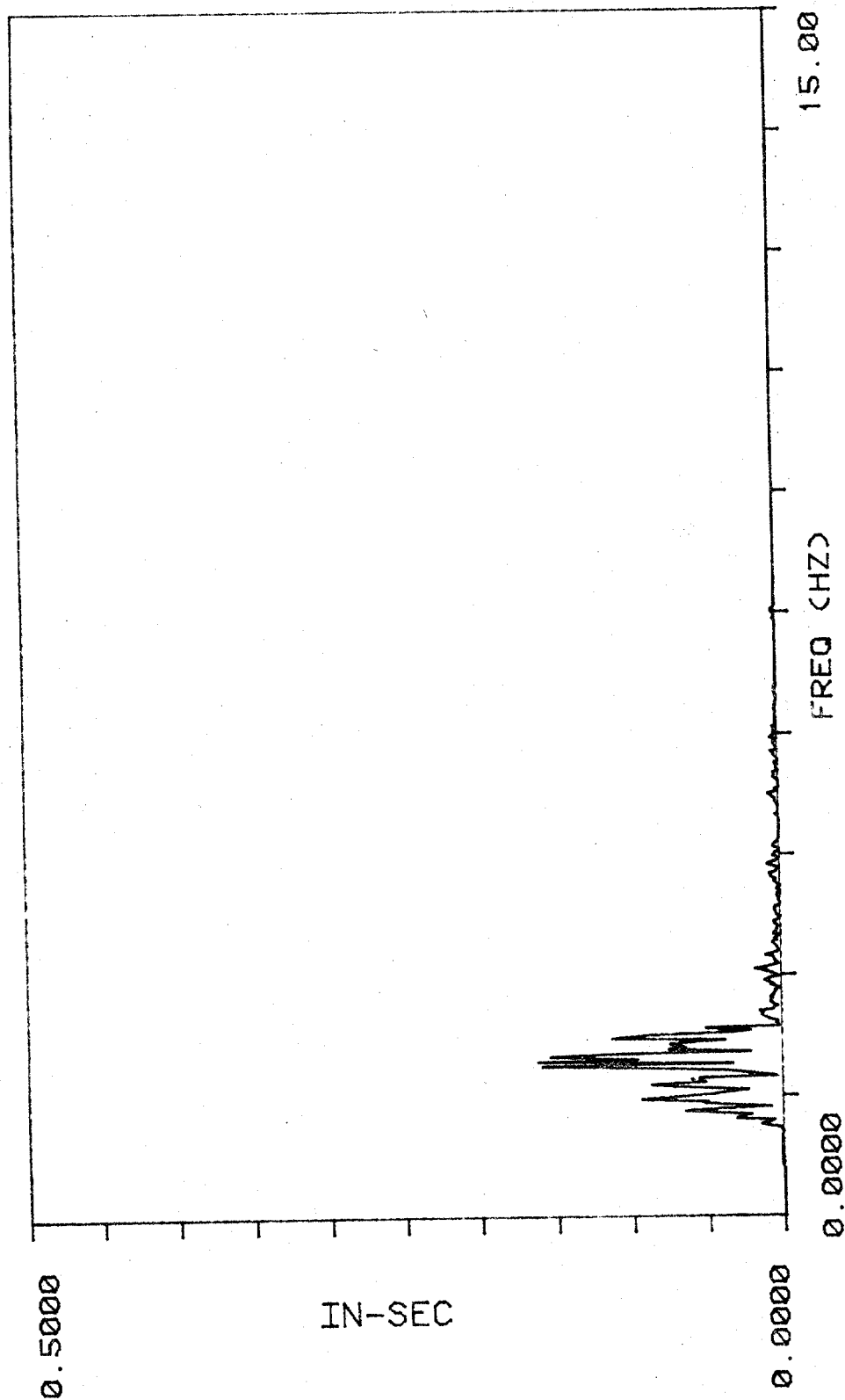THE PIPE AT NON-LOCK-IN AT L/8

39

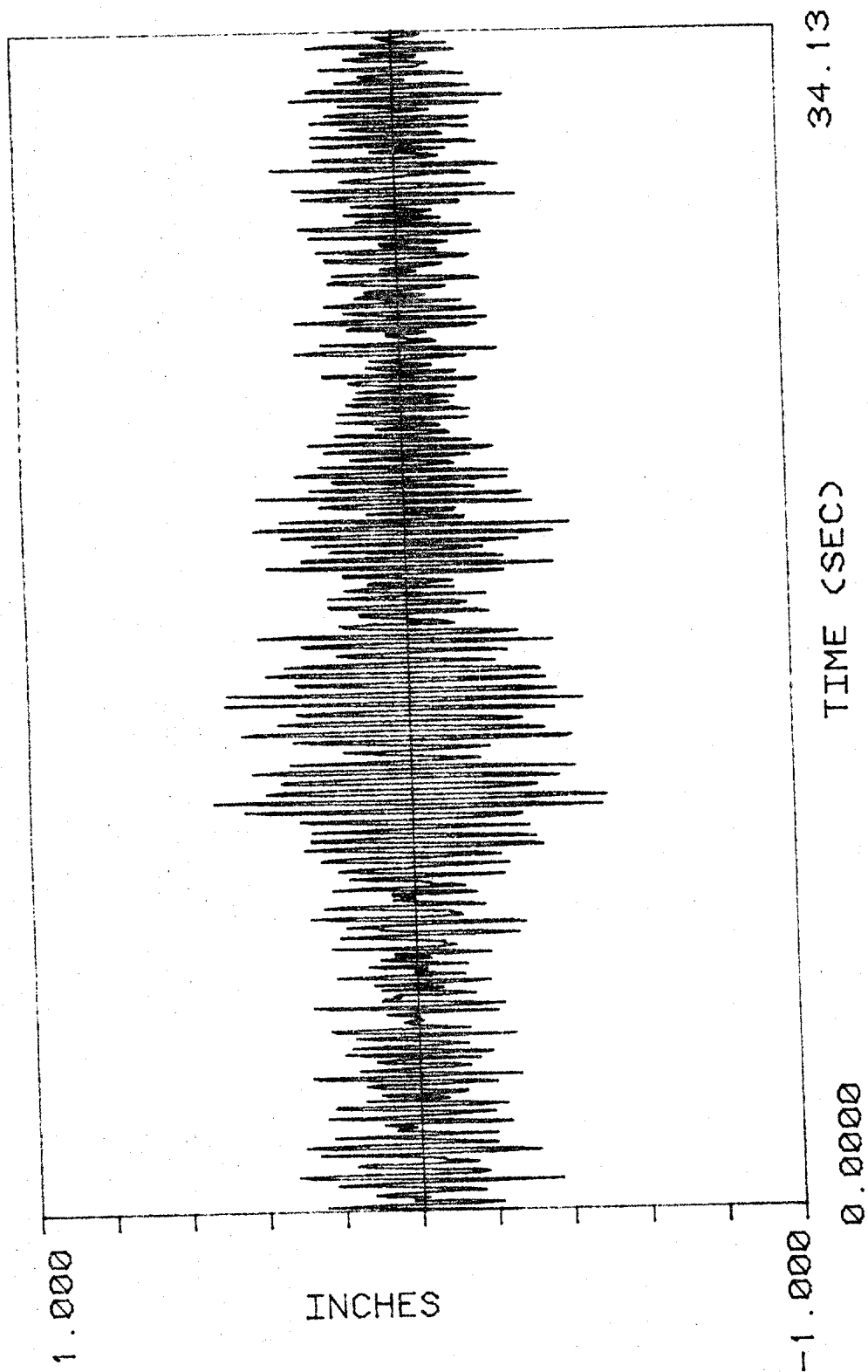FIG. 21 FFT OF THE VERTICAL DISPLACEMENT IN FIG. 20

40

FIG. 22   HORIZONTAL DISPLACEMENT OF THE
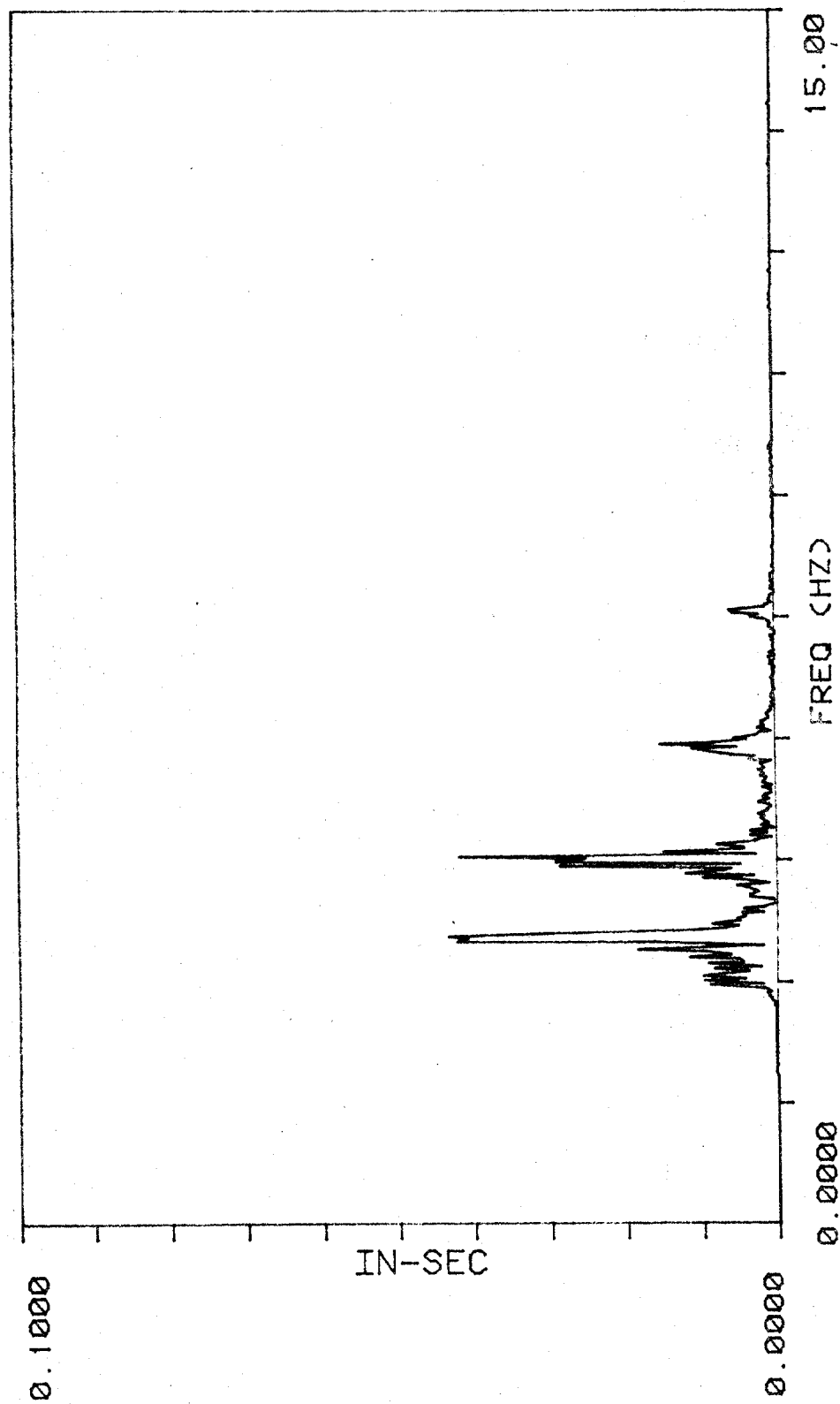
PIPE AT NON-LOCK-IN AT L/8

41

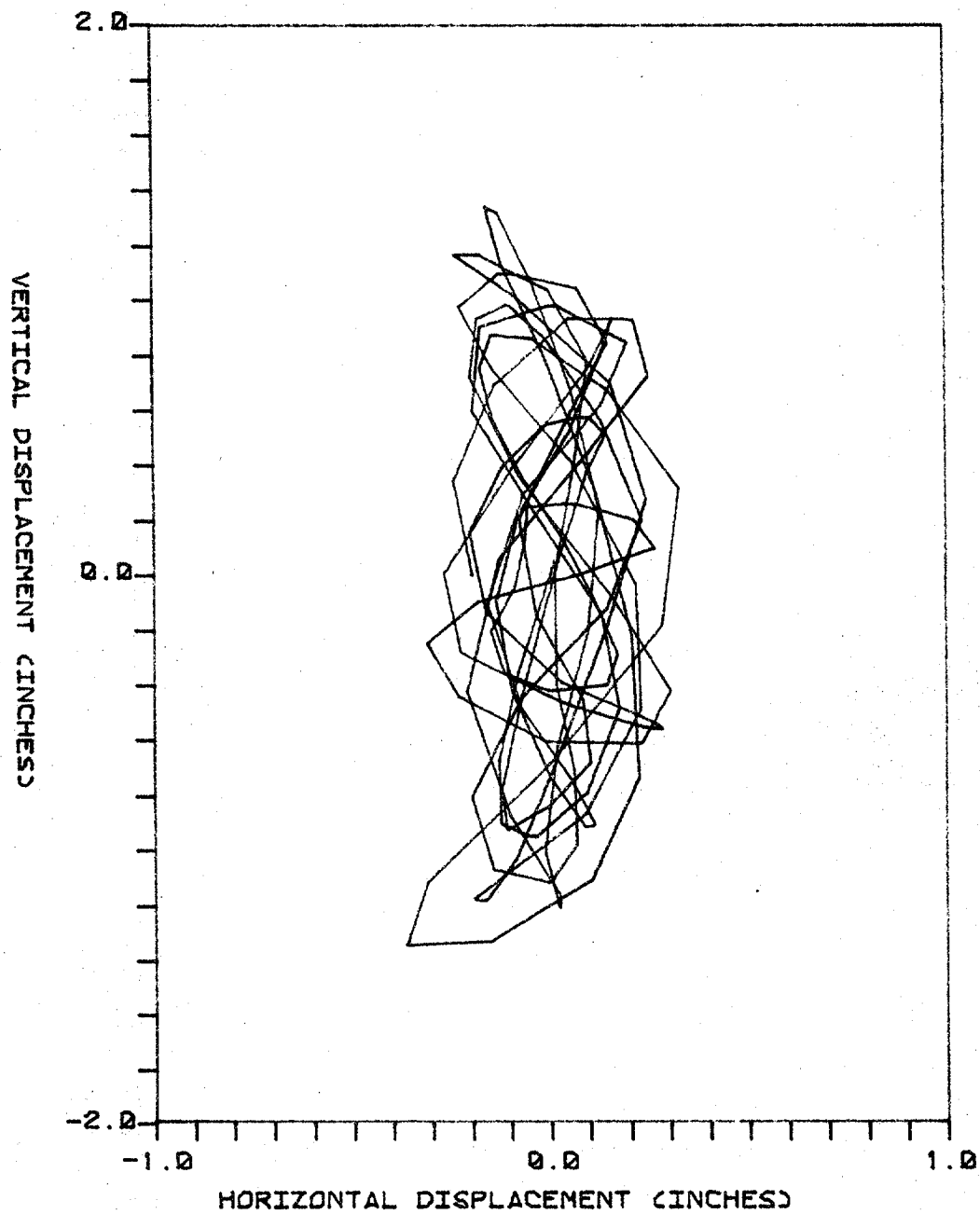FIG. 23 FFT OF THE HORIZONTAL DISPLACEMENT IN FIG. 22

42

FIG.24 TWO-DIMENSIONAL MOTION TIME
HISTORY OF THE PIPE AT NON-LOCK-IN
AT L/8

43

for complete 2 1/2-hour data acquisition cycles were
calculated for the pipe, bare cable, faired cable and a cable
with lumped masses. The RMS data were calculated by a moving
average whose window was 8.53 seconds in length. The
equation used was:

$$RMS = \cdot \sqrt{\frac{1}{N} \sum_{n=1}^{N} X^2 [n]} \qquad\qquad (4.3.1)$$

where N is 256 points and represents a time window of 8.53
seconds at a sampling rate of 30 HZ. These results are
presented in Figs. 25 to 28, along with linear moving average
values of drag coefficient and current speed. The
displacement data are taken from location 1/6 L for the pipe
and the bare cable, from location 3/4 L for the cable with
lumps and from location 2/5 L for the faired cable. These
are raw RMS displacements at the specified location and have
not been corrected for mode shape. Over the 2 1/2-hour test,
some periods correspond to lock-in responses, and others to
non-lock-in responses. As current speed falls within a
lock-in range, a substantial increase of vertical and/or
horizontal RMS displacement is observed. A corresponding
plateau in the drag coefficient is also observed. A more
complete analysis of the drag coefficient data is presented
in the thesis by McGlothlin (8). In that reference an
analysis of the errors in the drag coefficient calculation is
presented. A note of caution is appropriate here, the drag
coefficient data is least accurate at the very low-flow
speeds near the end of each test run. The drag coefficient
calculation requires division of drag force by velocity
squared. At low speeds these are both small numbers. At one
foot/second the error is approximately +15% dropping to + 10%
at 2.5 feet/sec. The high spike in the beginning of the drag
coefficient record in Figure 25 is due to a piece of seaweed
on the cable and should be disregarded.

FIG.25 2 1/2-HOUR RECORD OF THE DISPLACEMENT,
CURRENT AND DRAG COEFFICIENT FOR THE PIPE AT L/6
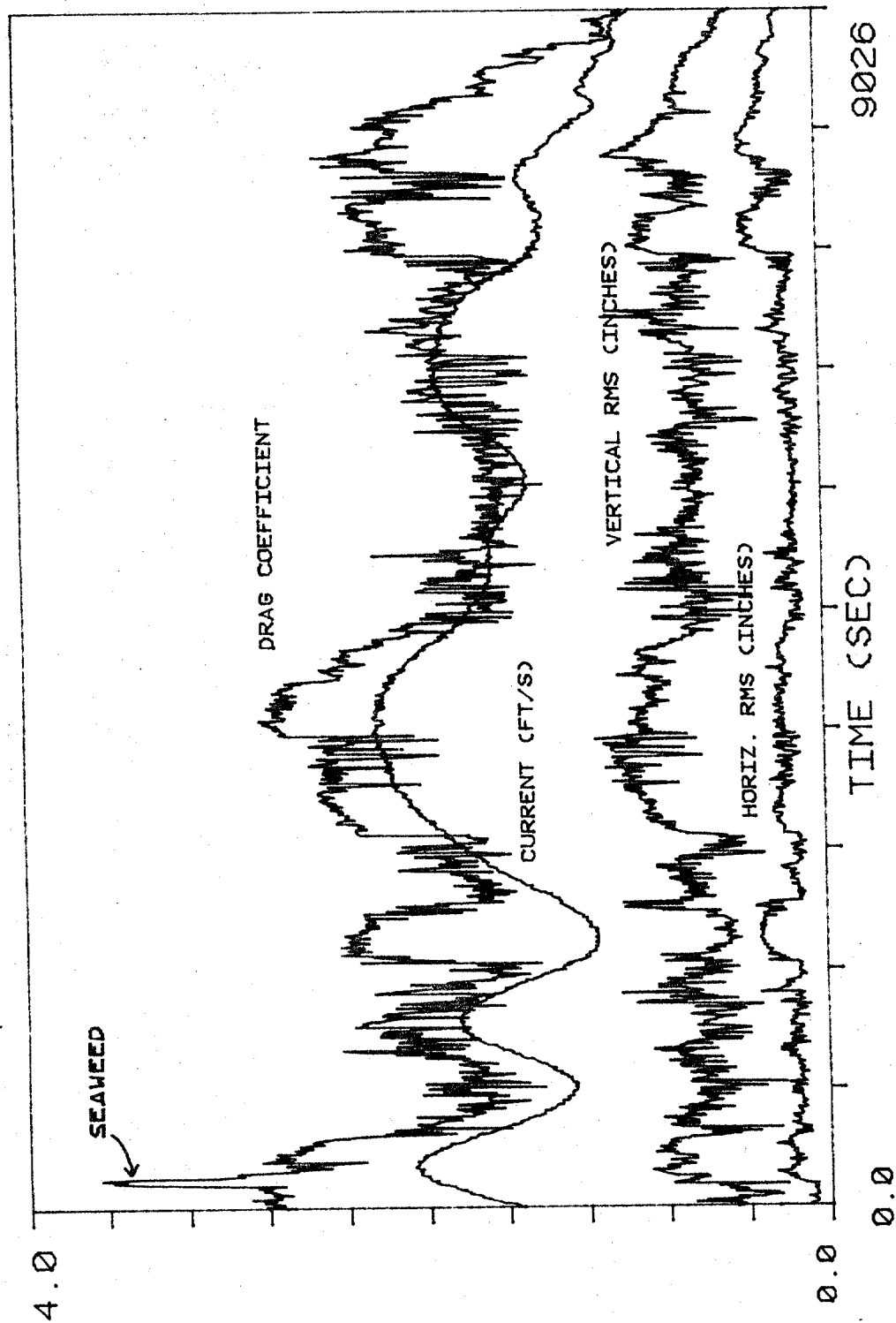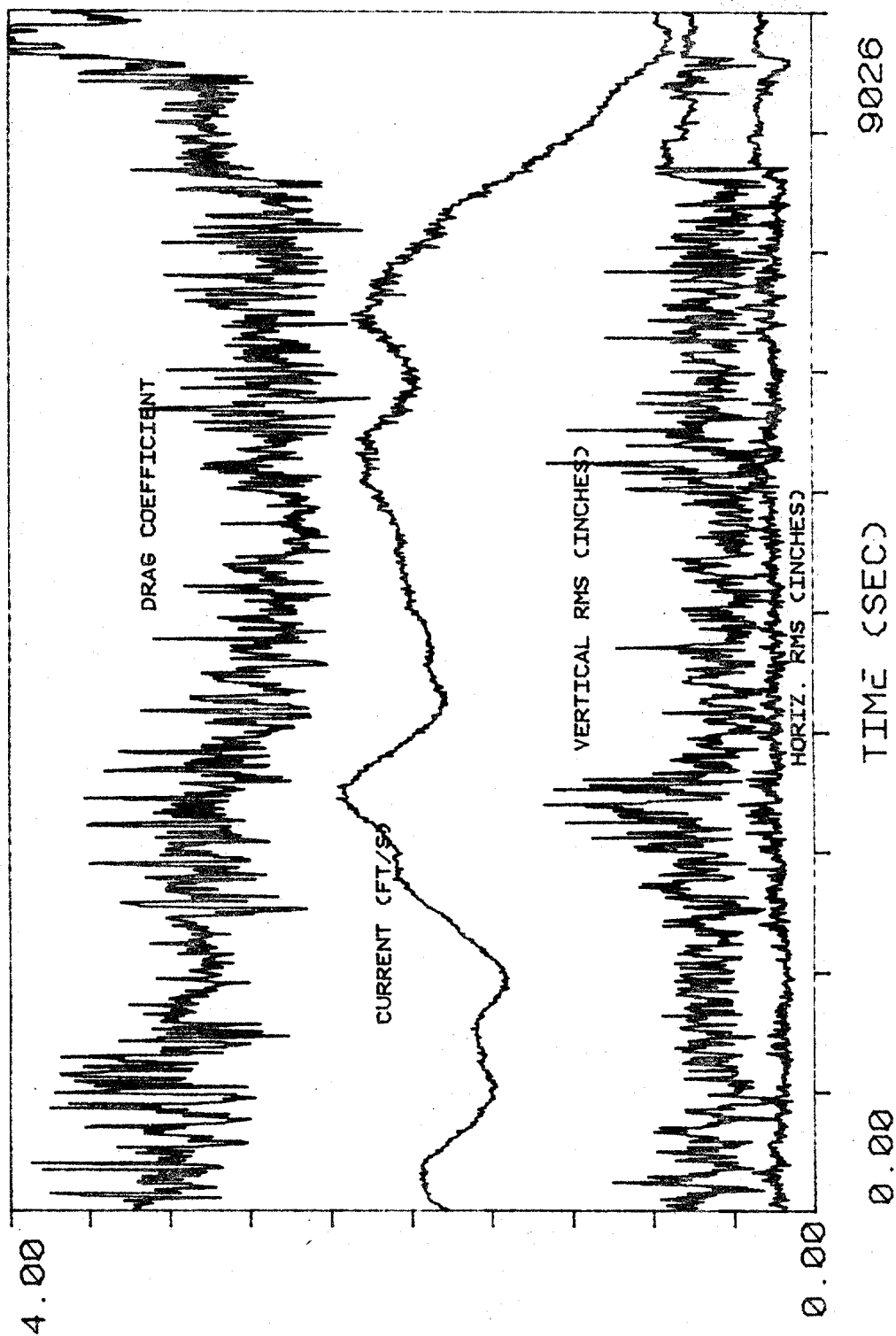
FIG. 26 2 1/2-HOUR RECORD OF THE DISPLACEMENT,
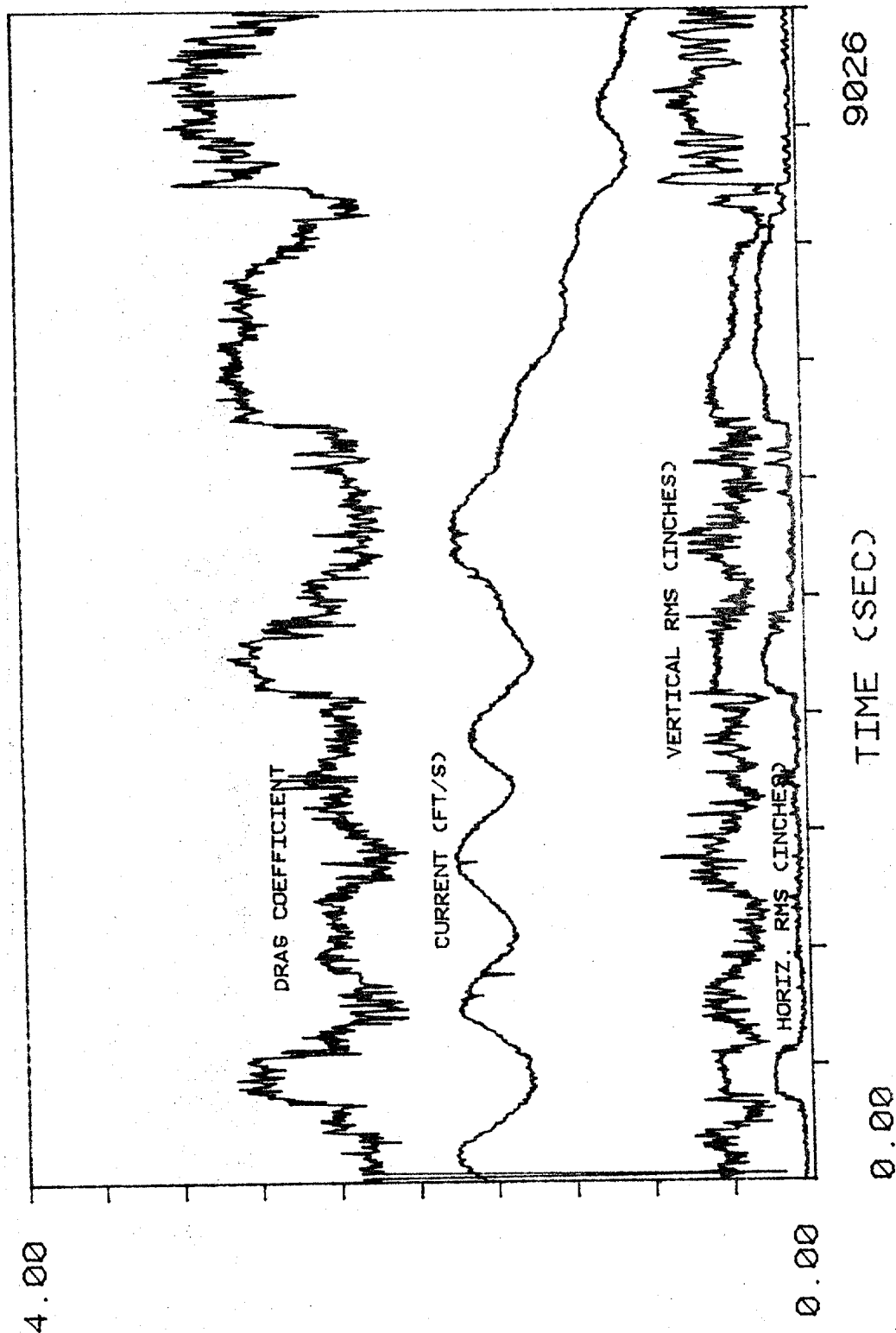CURRENT AND DRAG COEFFICIENT FOR THE BARE CABLE
AT L/6

FIG.27 2 1/2-HOUR RECORD OF THE DISPLACEMENT, CURRENT AND DRAG COEF. AT 3L/4 FOR THE CABLE WITH 2 LIGHT (L/6, L/2) AND 4 HEAVY (L/3, 5L/8, 3L/4, 7L/8) LUMPED MASSES
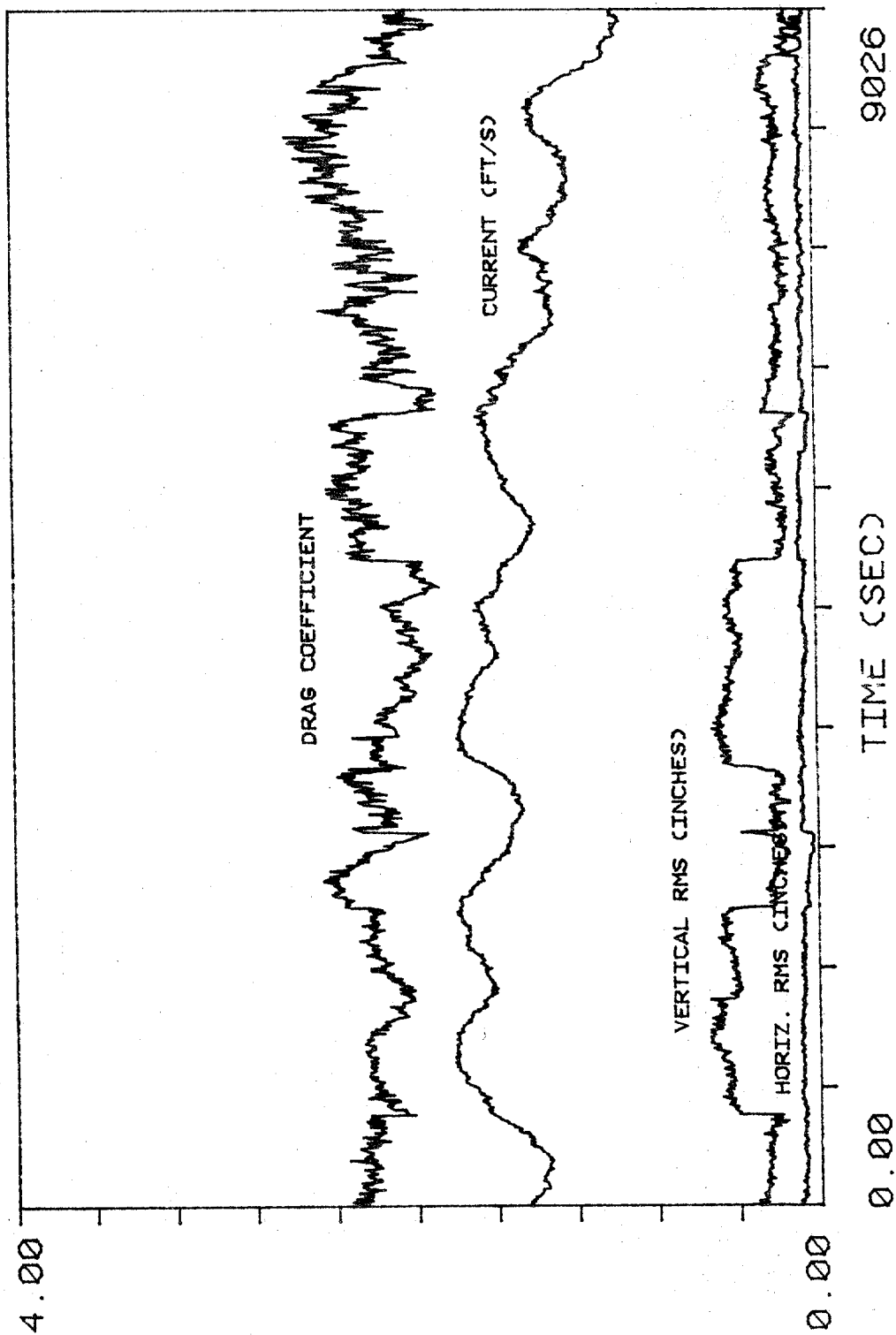
FIG. 28 2 1/2-HOUR RECORD OF DISPLACEMENT, CURRENT AND DRAG COEFFICIENT FOR THE FAIRED CABLE AT 2/5 L

48

CHAPTER 5
MODAL IDENTIFICATION

5.1 Modal Analysis

The response of a cylinder under external load can be described conveniently by using modal analysis. The method is intended to express the response as a superposition of the system's eigenfunctions multiplied by their corresponding time-dependent natural coordinates. As an illustration of this method, consider a uniform string under tensile load with pinned end boundary conditions. The equation of motion for this boundary value problem is:

$$Ty''(X,t) - R(X)\dot{y}(X,t) + f(X,t) = m(x)\ddot{y}(X_1 t) \qquad (5.1.1)$$

The response $y(x,t)$ may be expressed as a superposition of normal mode responses.

$$Y(X,t) = \sum_{r=1}^{\infty} Y_r(X)P_r(t) \qquad (5.1.2)$$

where $Y_r(x)$ is the normalized mode shape and has the following orthogonality property.

$$\int_0^{\ell} m(x) Y_r(x)Y_s(x) \, dx = \delta_{rs} \qquad (5.1.3)$$

Substitution of (5.1.2) into (5.1.1) multiplication by $Y_s(x)$, and integration from x=0 to L leads to:

$$\ddot{P}_r(t) + \dot{P}_r(t)\int_0^{\ell} R(x)Y_r(x)Y_s(x)dx + w_r^2 P_r(t) = N_r(t) \qquad (5.1.4)$$

If $R(x)$ is proportional to $m(x)$, orthogonality of normal modes leads to a set of uncoupled single degree of freedom oscillation equations in terms of the natural coordinates $P_r(t)$.

For $R(x) = C\, m(x)$ \qquad (5.1.5)

49

$$\ddot{P}_r(t) + c\dot{P}_r(t) + w_r^2 P_r(t) = N_r(t) \qquad (5.1.6)$$

where Nr(t) the modal force defined as:

$$N_r(t) = \int_o^\ell Y_r(x)\, f(x,t)\, dx \qquad (5.1.7)$$

In reality, the damping may not be governed by equation
5.1.5. However, for lightly damped well separated modes, the
uncoupled assumption yields good results. Such is the case
here. By an analogous derivation, the uncoupled normal mode
equations may be derived for a beam under tension, with
pinned end conditions. For a uniform beam the mode shapes
are sinusoids as they are for a uniform string. By using
modal analysis, the continuous system is reduced to many
single degree of freedom systems. In the next section we
will estimate the natural coordinate time histories, $P_r(t)$,
from measured responses at the accelerometer locations.

5.2 Estimation of Natural Coordinates

In the preceding section, the response of the cylinder was expressed in terms of a superposition of mode shapes $Y_r(x)$ multiplied by the natural coordinates $P_r(t)$:

$$y(X,t) = \sum_{r=1}^{\infty} P_r(t) \, Y_r(x) \qquad\qquad (5.2.1)$$

In this experiment, the response was measured at seven positions. They are at 1/8L, 1/6L, 1/4L, 2/5L, 1/2L, 5/8L, 3/4L. In this study a least squares method was used to estimate the natural coordinates in terms of the measured responses at these seven positions. For any test case the response is dominated by a finite number of modes usually 2 to 6 in number. A first guess at the responding modes may be obtained by inspection of the response spectrum at any one location. By summing the normal mode responses over the apparent participating modes, the following equations are obtained, where the range M~N covers all of the participating modes. The mode shapes can be calculated theoretically. For the pin-supported uniform cylinder, the mode shapes are given by

$$Yr(x) = \sin(r\pi x/L)$$

At time t=to, the response of position $x=X_j$ can be expressed as:

$$Y(X_j, t_o) = \sum_{i=m}^{N} P_i(t_o) Y_i(X_j) + E(X_j) \qquad\qquad (5.2.2)$$

where $E(X_j)$ is the noise term.

Rewriting (5.2.2) in matrix form:

$$\{y\} = [Y] \{P\} + \{E\} \qquad\qquad (5.2.3)$$

where y_j is the vector of the measured response

Y_{ij} is the mode shape matrix

P_i is the vector of the natural coordinate

E_j is the vector of noise (or error)

$i=m,N \qquad j=1,7$

The sum of error squares ee is given by

$$ee = <E> \{E\} = \{y\} - [Y]\{P\}\}^T\{\{y\}-[Y]\{P\}\}$$

$$= \{y\}^T\{y\} - 2\{P\}^T[Y]^T\{y\} + \{P\}^T[Y]^T[y]\{P\} \quad (5.2.4)$$

The vector of natural coordinates Pi is to be determined such that the error squared term is minimized.

$$\min[ee] = \min[\{E\}^T\{E\}]$$

Let

$$\frac{d}{dP_i} (ee) = 0 \qquad\qquad (5.2.5)$$

and solve for P(t).

$$\{P\} = [[Y]^T[Y]]^{-1}[Y]^{-1}\{y\} \qquad\qquad (5.2.6)$$

or

$$\{P\} = [T] \{y\} \qquad\qquad (5.2.7)$$

where [T] is the transfer matrix:

$$[T] = [[Y]^T[Y]]^{-1}[Y]^T \qquad\qquad (5.2.8)$$

Equation (5.2.7), decomposes the measured response at the seven positions into the natural coordinates provided the mode shapes are known and the guess of the responding modes is initially correct. Figure 22 showed an example of the horizontal pipe vibration displacement at position L/8. It is clear that several modes were excited. In the displacement spectrum, there are several peaks, each corresponding to one particular mode to be identified. Using the method discussed above, the natural coordinate time histories were obtained for the 4th, 5th, 6th and 7th modes corresponding to each peak in the displacement spectrum, shown in Fig. 23. These natural coordinate time histories are shown in Fig 29. The FFT of fourth- and fifth-mode natural coordinates are shown in Figs. 30 and 31. Each natural coordinate time history represents the antinode displacement for that mode. Their sum does not equal the displacement portrayed in Fig. 22 because it is the motion at a specific point on the cable.

5.3 Response Mode of In-line Motion at Lock-in

In Chapter 4 it was stated that at lock-in the in-line response is at twice the frequency of the cross-flow. The question arises, what mode responds in the in-line direction. These modal identification techniques have been used to provide the answer, with some very surprising results. One
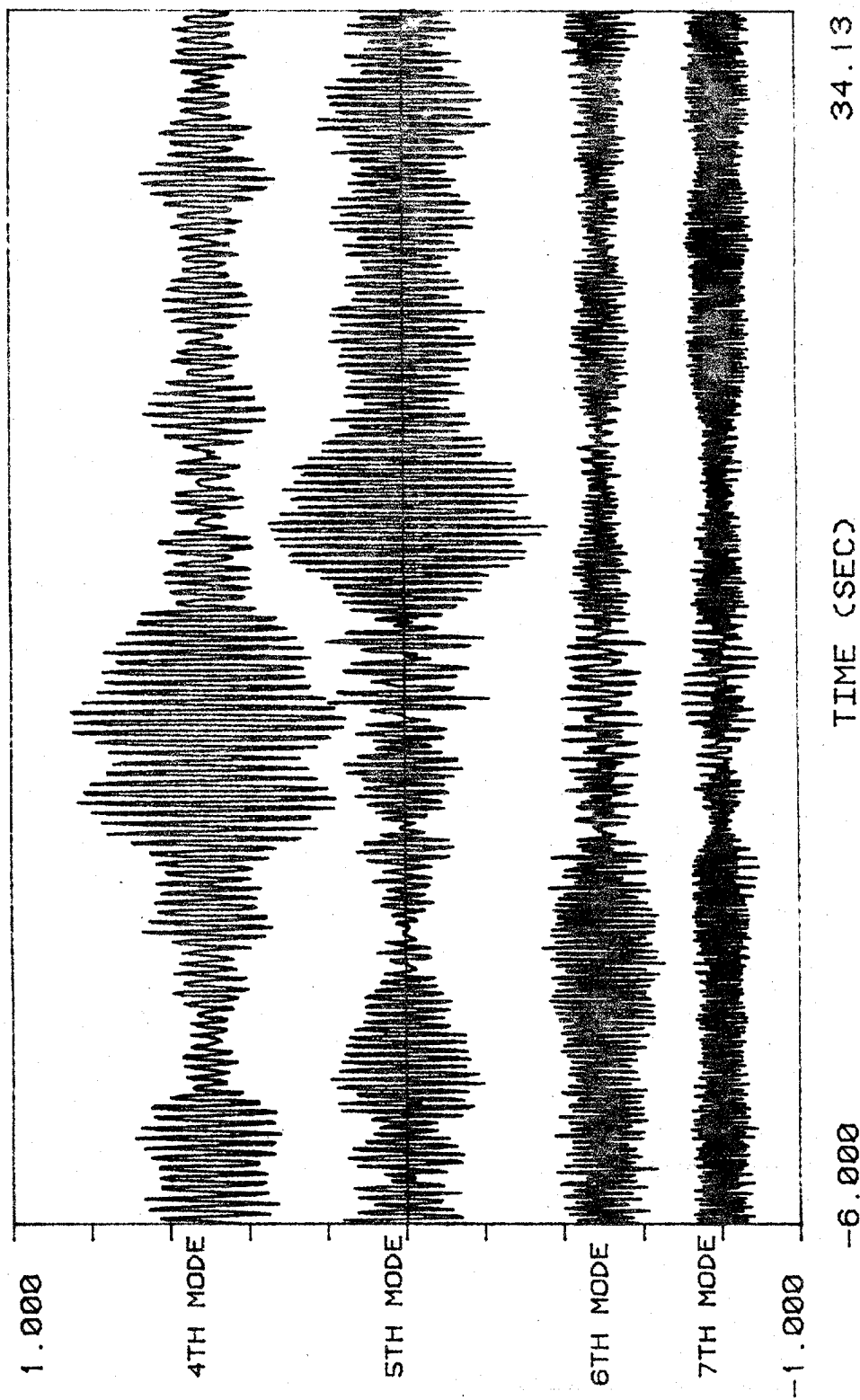
53

FIG. 29   NATURAL COORDINATE TIME HISTORIES FOR THE 4TH,
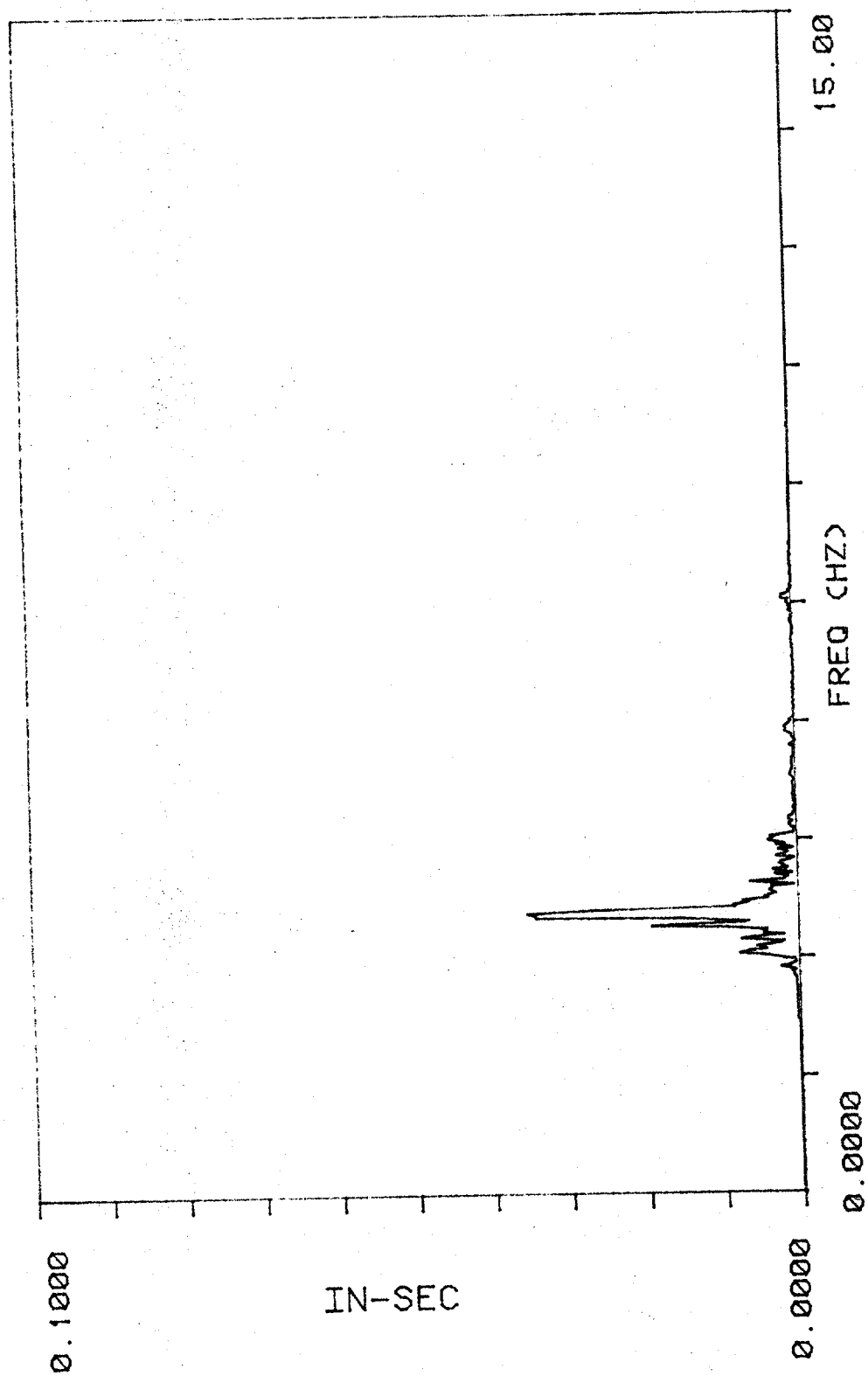5TH, 6TH, AND 7TH MODES OF THE PIPE

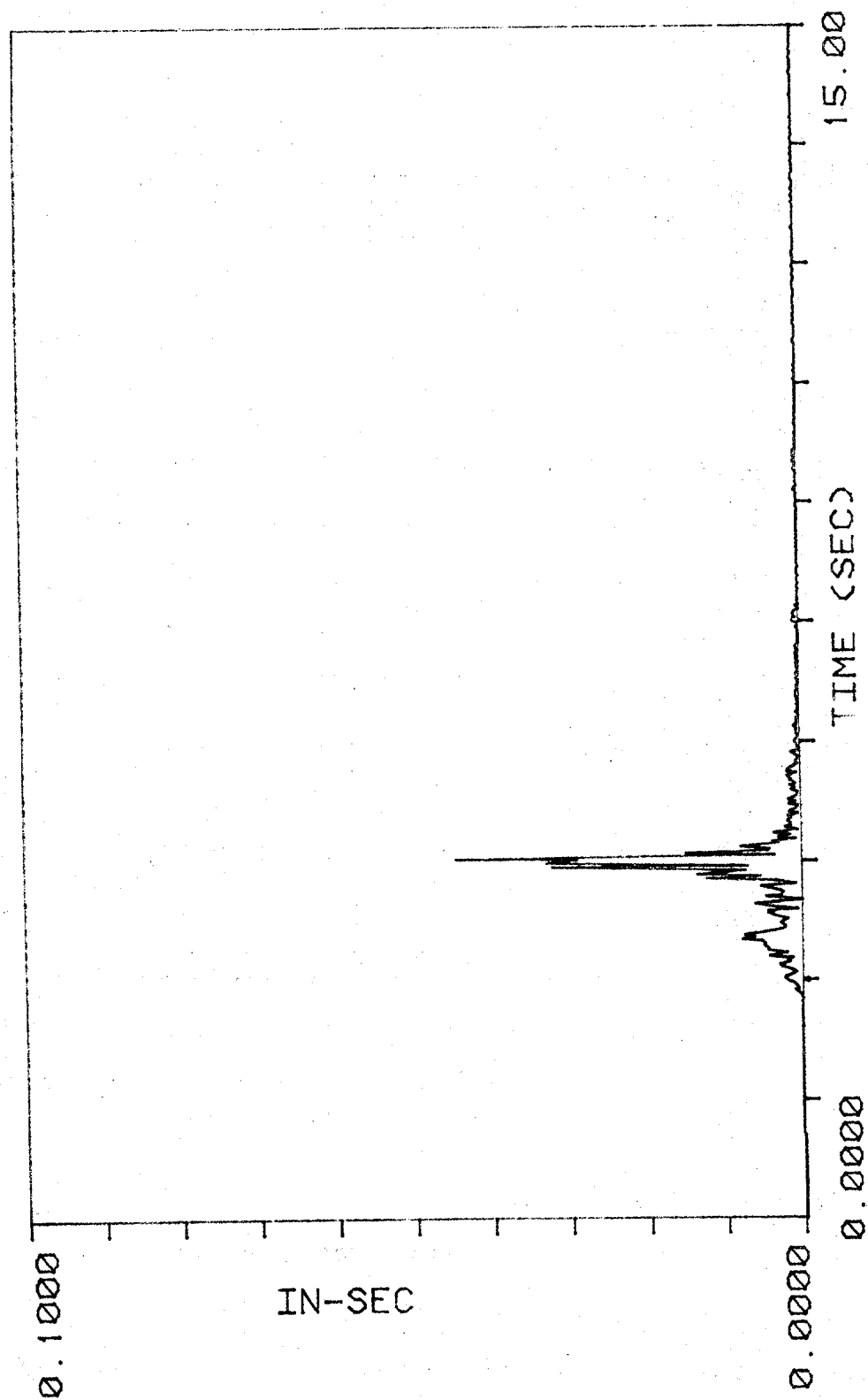54

FIG.30 FFT OF THE 4TH NATURAL COORDINATE TIME HISTORY

FIG. 31 FFT OF THE 5TH NATURAL COORDINATE TIME HISTORY

such interesting case as described below.

For a taut cable,all of the natural frequencies are integer multiples of the lowest. Therefore it is reasonable to expect that the fluctuating drag forces will excite an in-line mode whose natural frequency is twice that of the mode which is responsible for the cross-flow lock-in. As will be shown, this is often not the case. Figures 32 through 35 are the displacements and FFT's of the cable in the vertical and horizontal directions at L/8. The cross-flow motion is at the second-mode natural frequency of the cable, and the in-line motion is at the fourth-mode natural frequency. Least squares modal identification was carried out in both directions and the resulting natural coordinates revealed that the vertical vibration was in the second-mode shape, while the horizontal vibration was in the third-mode shape instead of the fourth-mode as had been expected. The frequency of this third mode motion was not the natural frequency of the third mode but was in fact equal to the natural frequency of the fourth mode. The response was not resonant, but inertia controlled response of the third mode. Why was there no resonant response in the fourth mode? A close look at the fluctuating drag forces provides the explanation. For all pin-ended, uniform cylinders in a uniform flow, lock-in with cross-flow vibration modes generates fluctuating drag forces which are symmetrically distributed about the center of the cylinder. The resulting modal exciting forces are given by equation 5.1.7. If a mode
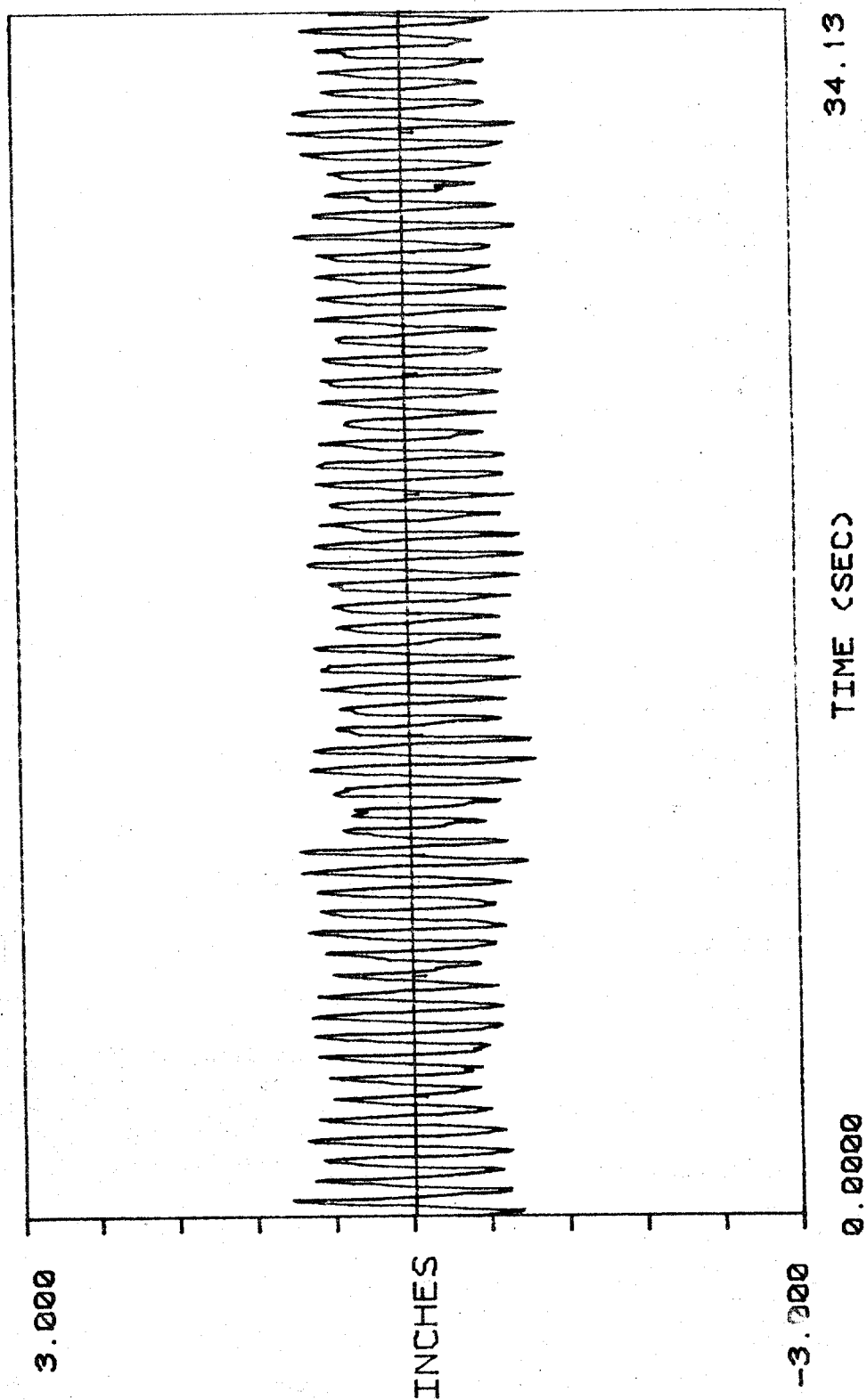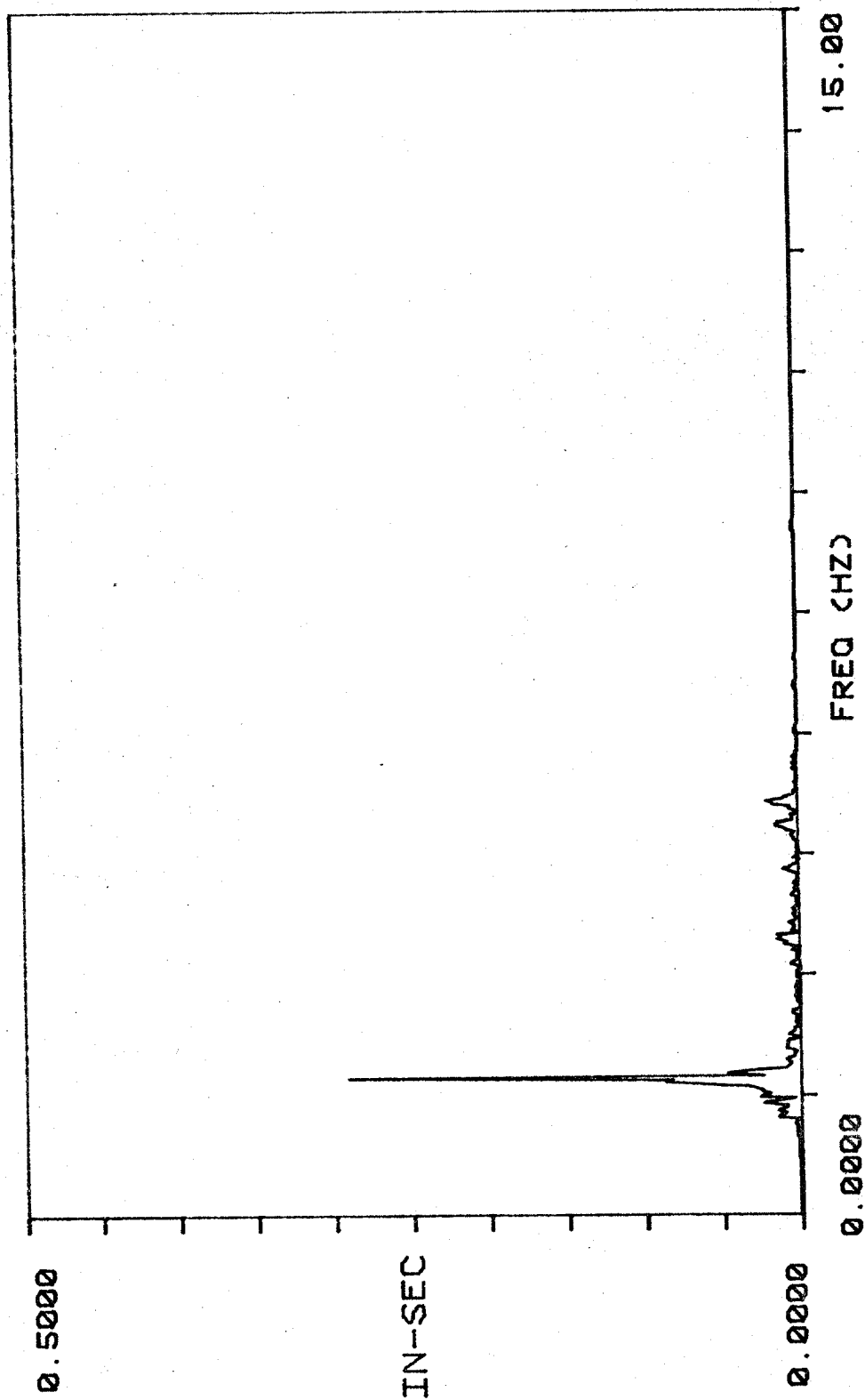
FIG. 32 CROSS-FLOW DISPLACEMENT OF THE CABLE
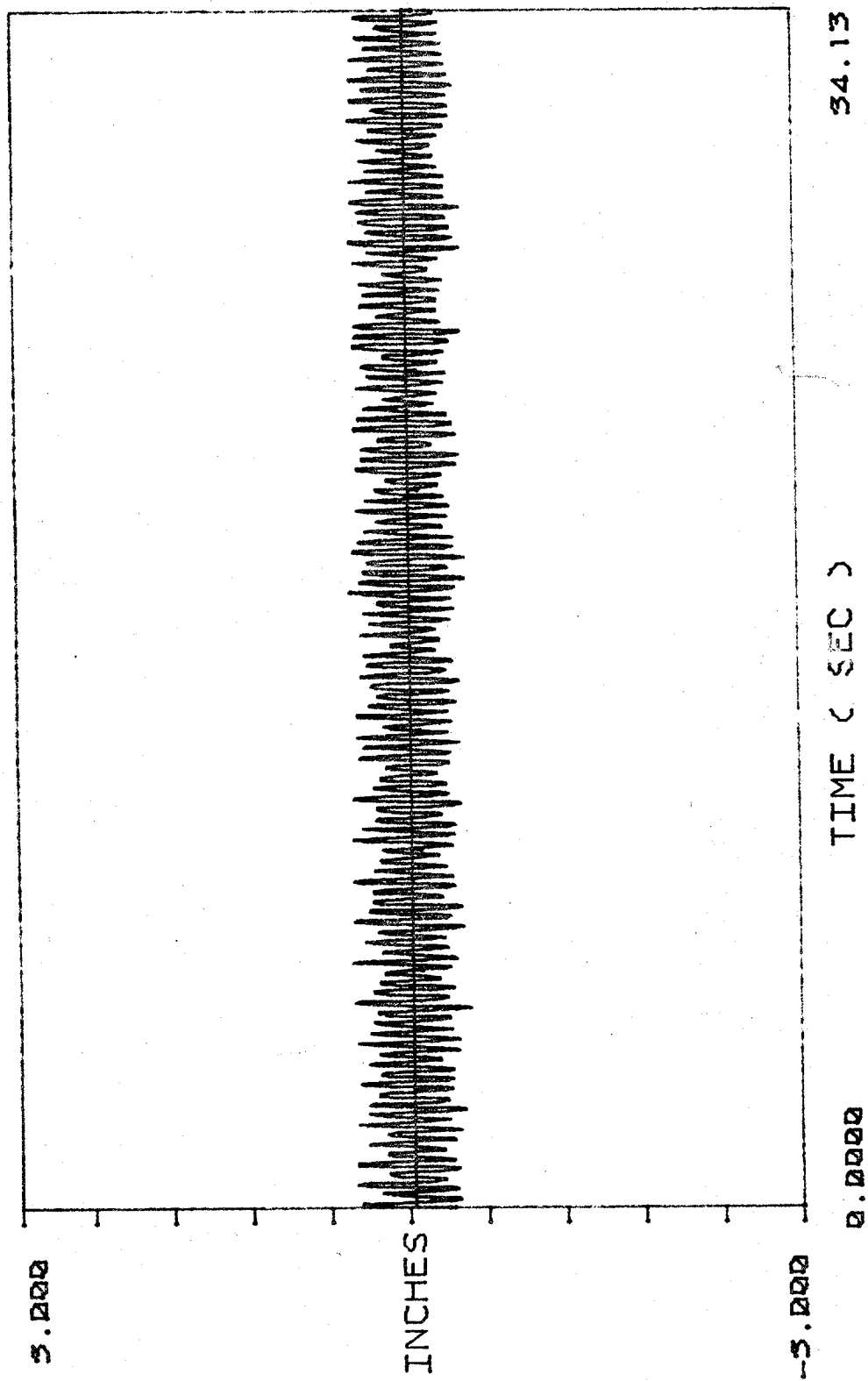AT L/8

FIG.33 FFT OF THE CROSS-FLOW DISPLACEMENT IN FIG.32
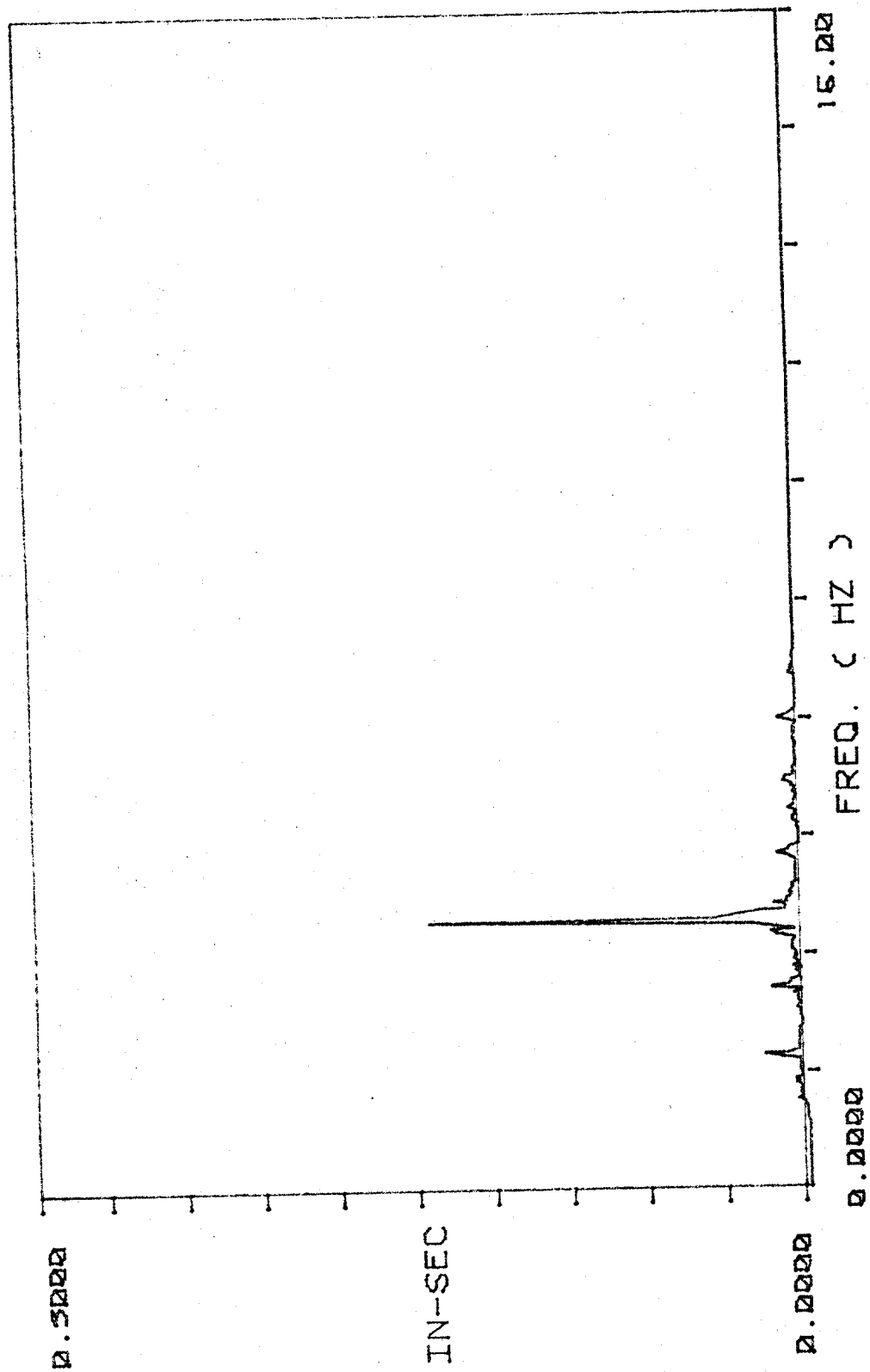
FIG. 34 IN-LINE DISPLACEMENT OF THE CABLE
AT L/8

60

FIG.35 FFT OF THE IN-LINE DISPLACEMENT IN FIG.34

61

shape is asymmetric with respect to the center of the cylinder, this integral and hence the modal force are zero. If the mode shape is a symmetric function with respect to the center, the integral and resulting modal force are non-zero. For cables and pipes under tension with pinned ends, the even-numbered modes are asymmetric and, hence, cannot be excited. The odd-numbered modes are symmetric with respect to the center and may be excited. In this particular case, even though the excitation was near the natural frequency of the fourth in-line mode, the modal force of the fourth mode was zero. The observed response was principally in the third mode. Figure 36 shows the natural coordinates of different modal participations in displacement in the horizontal direction.

5.4 RMS Response in the Natural Coordinates During Non-lock-in

Lock-in responses can be described by periodic deterministic models. Non-lock-in has a much more random character. At constant current speed and non-lock-in conditions, the participation of the contributing modes varies with time. An example of this spanning a very short period of time was presented in Fig. 29, in the section on modal coordinate identification. It is enlightening to study non-lock-in response on a longer time scale. A 448-second record of non-lock-in pipe response was analyzed and the natural coordinate contributions were separated by the methods described previously. Moving average RMS natural
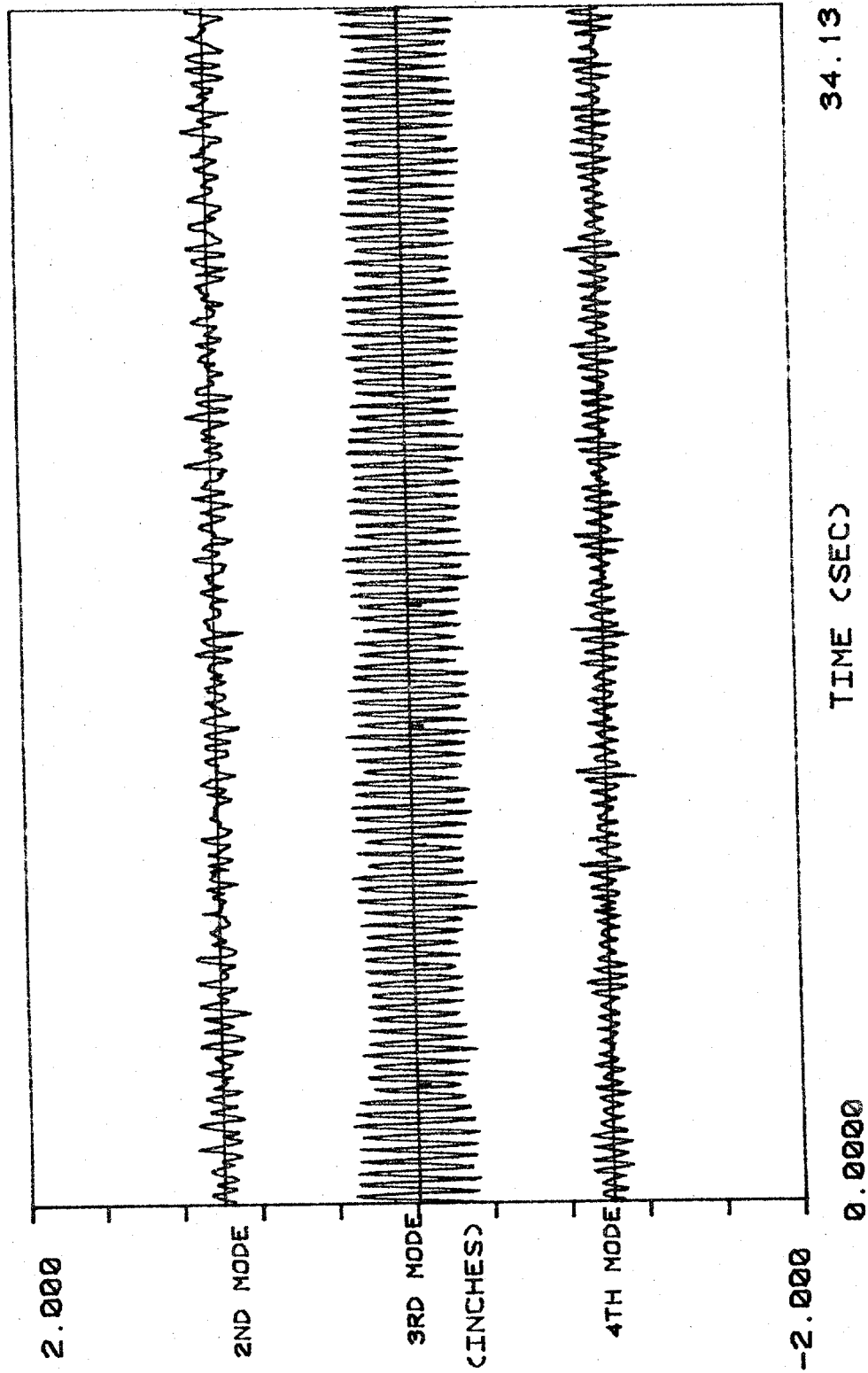
FIG.36 IN-LINE NATURAL COORDINATE TIME HISTORIES
FOR 2ND. 3RD. AND 4TH MODES OF THE CABLE

coordinate responses were calculated. These are plotted in
Figs. 37 and 38. These responses reflect the RMS values of
the individual modal anti-node responses. The current and
drag coefficient for the same time interval is shown in Fig
39. The total response stays approximately constant while
the individual modal contributions vary over wide ranges. As
one mode recedes, another appears to take its place.

FIG.37 RMS OF THE NATURAL COORDINATES
FOR THE 2ND, 3RD, 4TH AND 5TH
CROSS-FLOW MODES OF THE PIPE

65

FIG.38 RMS OF THE NATURAL COORDINATES
FOR 3RD, 4TH, 5TH, 6TH AND
7TH IN-LINE MODES OF THE PIPE

66

FIG.39 DRAG COEFFICIENT AND CURRENT
CORRESPONDING TO FIG.37 AND 38

CHAPTER 6

CONCLUSION

The following conclusions may be made based on the test data presented:

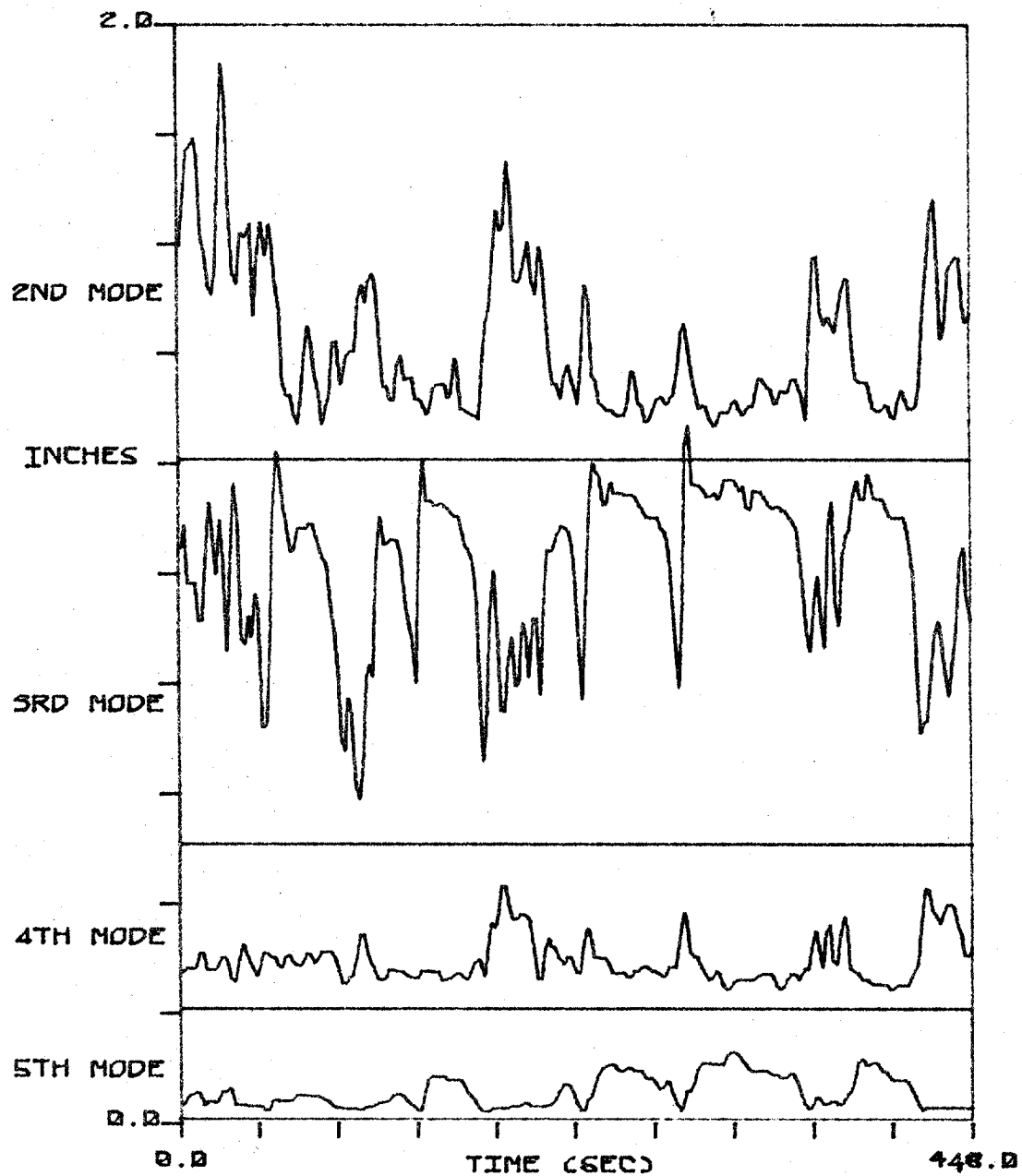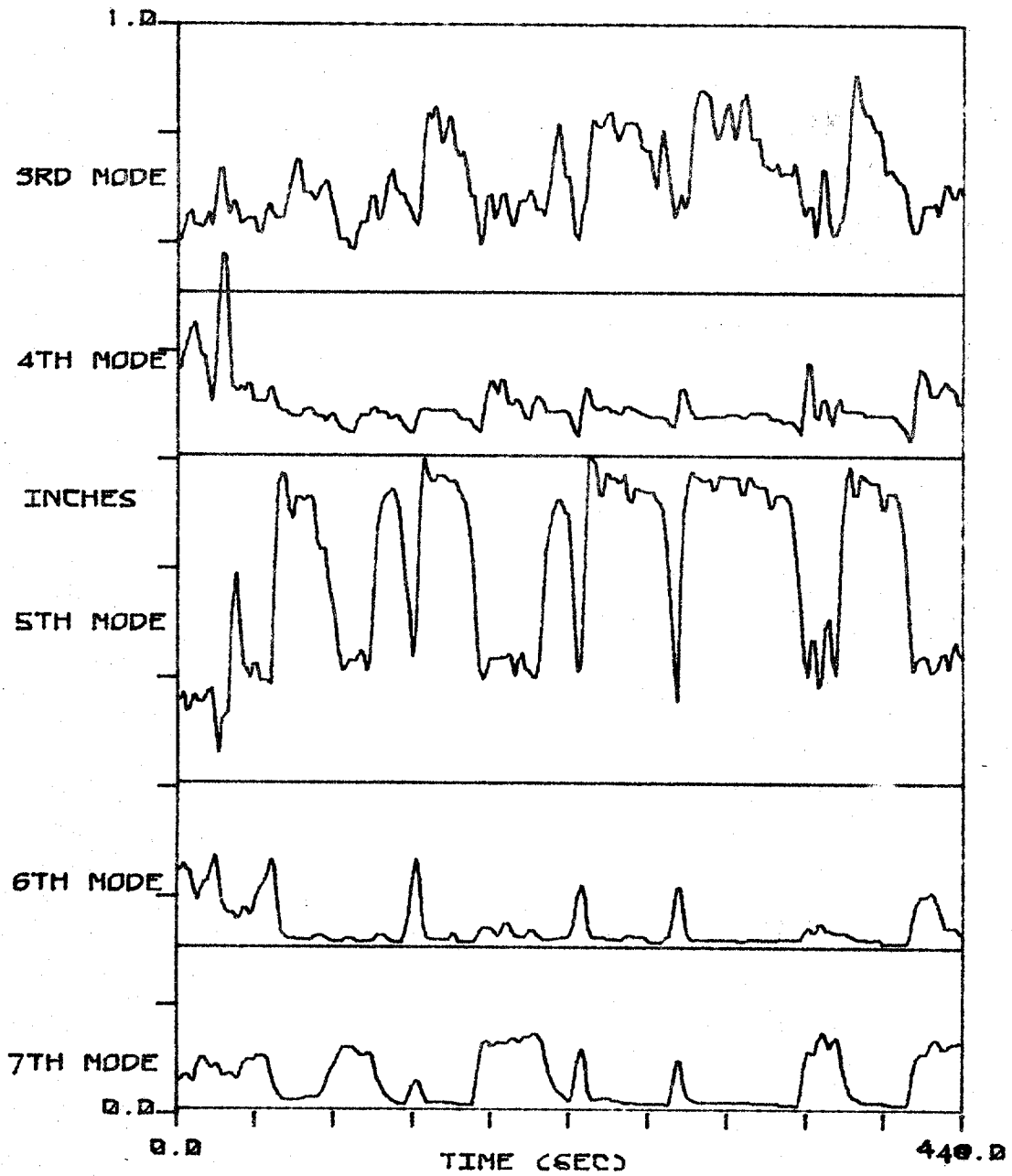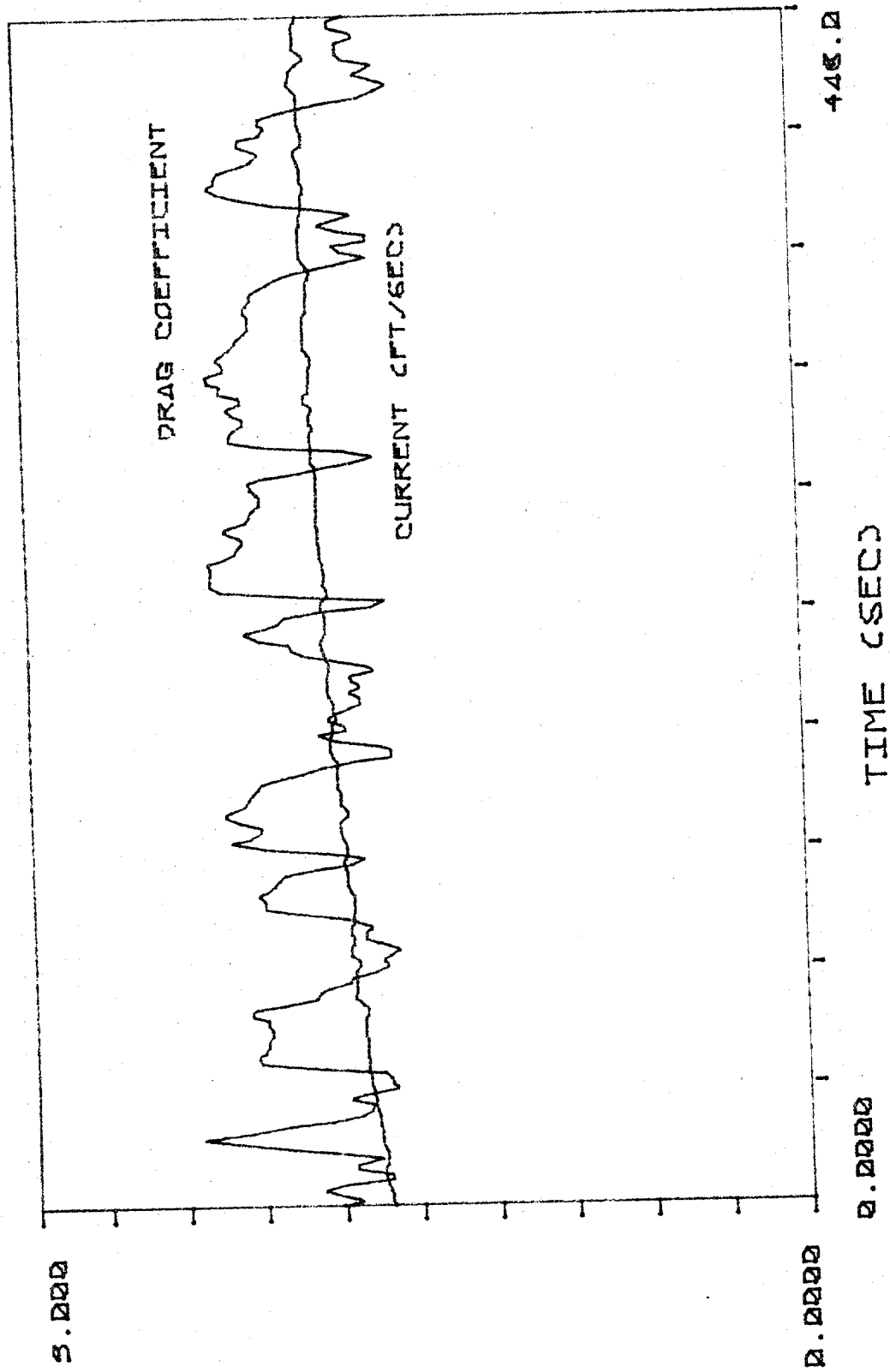i.   At lock-in, the transverse motion is characterized by single-mode response. The in-line motion may have two modes: the dominant one has a frequency twice that of the transverse frequency and need not be the resonant response of any particular mode, the smaller in-line response component is at the frequency of the cross flow vibration and represents a small amount of resonant in-line vibration which is driven by unknown coupling mechanisms to the cross flow vibrations. Motion time histories at lock-in are deterministic. The phase between the in-line and cross-flow components occasionally results in figure 8 patterns (as in Fig. 19). Many other repeating patterns have been observed, depending on the position on the cable and the principal responding mode. The amplitude of transverse response is about twice that of the in-line motion. A narrow band periodic lift force is implied.

ii. At lock-in, the in-line response is at twice the frequency of the transverse motion. The responding in-line mode shapes are symmetric with respect to the center of the cylinder. Asymmetric modes are excited very little due to the symmetric distribution of the drag exciting forces.

iii. At non-lock-in, several modes respond in both in-line
     and transverse directions, and the center frequency of
     the in-line motion is higher than that of the
     transverse. Wide-band lift and drag forces are implied.

iv. At non-lock-in ,vibration energy can transfer from one
     mode to another mode without any significant change in
     current speed as shown in Fig. 29.

v.   Maximun drag coefficient occurs at lock-in, and is about
     3.0 for the pipe, and 3.3 for the bare cable as shown in
     the 2 1/2-hour RMS data. Maximum RMS transverse and
     in-line displacements also occur at lock-in. However,
     peak responses are usually higher in the non-lock-in
     motion.

REFERENCES

1. Basili, M. and Brady A.G. "Low Frequency Filtering and The Selection of Limits for Accelerogram Coefficients", Proc. of the Sixth European Conference on Earthquake Engineering, Yugoslavia, 1978.

2. Bendat,J.S. and Piersol, A.G., Random Data: Analysis and Measurement Procedures, John Wiley and Sons, New York, 1971.

3. Blevins, R.D., Formulas for Natural Frequency and Mode Shape, Van Nostrand Reinhold Company, New York, 1979.

4. Clough, Ray W. and Penzien, Joseph, Dynamics of Structure, McGraw-Hill, New York, 1975.

5. Gray, A.H., and Markel J.D. "A Computer Program for Designing Digital Elliptic Filters", IEEE Trans. on Acoustics, Speech, and Signal Processing, December 1976.

6. Hamming R.W., Numerical Methods for Scientists and Engineers, McGraw-Hill Co. New York, 1962.

7. King, R., "A Reveiw of Vortex Shedding Research and Its Application", Ocean Engineering, New England Section, Sept. 26, 1975.

8. McGlothlin J.C. "Drag Coefficients of Long Flexible Cylinders Subject to Vortex Induced Oscillation", Thesis Presented to the Massachusetts Institute of Technology, Cambridge, Mass. 1981.

9. Meirovitch, Leonard, Analytic Method in Vibrations, MacMillan Co., New York, 1967.

10. Oppenheim, A.V. and Schafre R.R., Digital Signal Processing, Prentice-Hall, Inc., Englewood Cliffs, N.J. 1975.

11. Rabiner, L.R. and Gold B., Theory and Application of Digital Signal Processing, Prentice-Hall, Inc. Englewood Cliffs, N.J. 1975.

12. Sarpakaya. T., "Vortex Induced Oscillations. A Selective Review." ASME Journal of Applied Mechanics, Vol. 46, June 1979, pp. 241.

13. Schuessler, H,W. and Ibler, W. "Digital Filters for Integration", European Conference on Circuit Theory and Design, Institute of Electrical Engineers, Conference Publication No. 116, 1974.

14. Skop, R.A., Griffin, O.M. and Ramberg, S.E ., "Strumming Predictions for the SEACON II Experimental Mooring," Proc. Offshore Tech. Conf., Houston, Texas, OTC 2884, 1977.

15. Trifunac, M.D. and Lee V.W. "Uniformly Processed Strong Earthquake Ground Accelerations in the Western United States of America for the Period from 1933 to 1971: Corrected Acceleration, Velocity and Displacement Curve", Report No. 78-01 Dept. of Civil Eng., U. of S. California, CA.

16. Vandiver J.K. and Griffin O.M. "Measurement of the Vortex Excited Strumming Vibrations of Marine Cables," Proc. of Ocean Structural Dynamics, 982.

17. Vandiver J.K. "Natural Frequency, Mode Shape, and Damping Ratios for Cylinders Tested at Castine," unpublished M.I.T. Ocean Engineering Report.

18. Vandiver J.K. and Mazel, C.H. , "A Field Study of Vortex-Excited Vibrations of Marine Cable", Offshore Tech. Conf., Houston, Texas, OTC 2491, 1976.

APPENDIX 1

CASE STUDY

A case study for double integrating an acceleration time series is described here:

(1) Fig. A.1 shows the acceleration time histories to be double integrated.

(2) The first step is to obtain the theoretical FFT of diaplacement and then determine the stop-band and pass-band edge frequencies Fig. A.2 shows the theoretical FFT of displacement, from which we have:

    Ws = 1.7 Hz
    Wp = 2.0 Hz

(3) Determine the pass-band and stop-band ripple tolerance Ps and Pp. A typical value for Ps and Pp in the data processing presented here are:

    Ps=0.01
    Pp=0.01

(4) Determine the order of the filter N from design charts (10). For this case study:

    N=8

(5) Calculate the positions of poles and zeros and the cascade form filter coefficients from the computer program IIR. The following parameters are obtained for the high-pass filter.

pole locations:

0.905654 + i 0.397566

0.862657 + i 0.407297

0.739515 + i 0.425226

0.419697 + i 0.286726

zero locations:

0.938481 + i 0.345329

0.948841 + i 0.315753

0.971191 + i 0.924658

(6) Carry out all eleven steps described in section 3.5 in the computer program LLITG, and the final displacement are obtained as shown in Fig. A.3 and Fig. A.4.

The programs IIR and LLITG are interactive in nature and begin with a series of queries which must be responded to by the user in order to proceed with the program. Pages 78 and 79 give the queries and the answers as used in the example in this appendix. Pages 80 and 81 give additional explanation regarding the information required in response to each of the queries. With this report, the example in the appendix and a listing of the programs the reader should be able to assemble a set of programs for the double integration of time series data. Program listings will be provided on request.
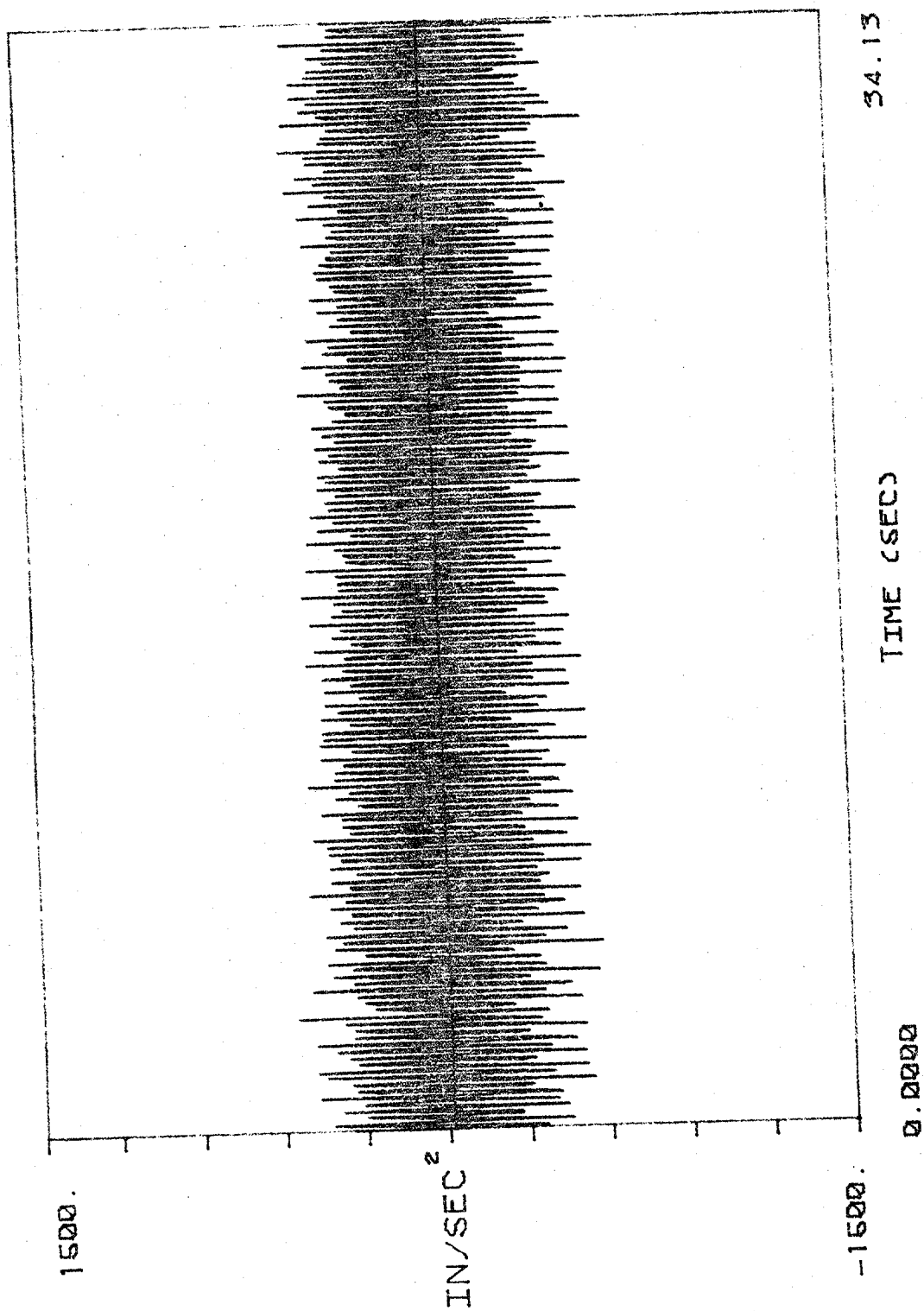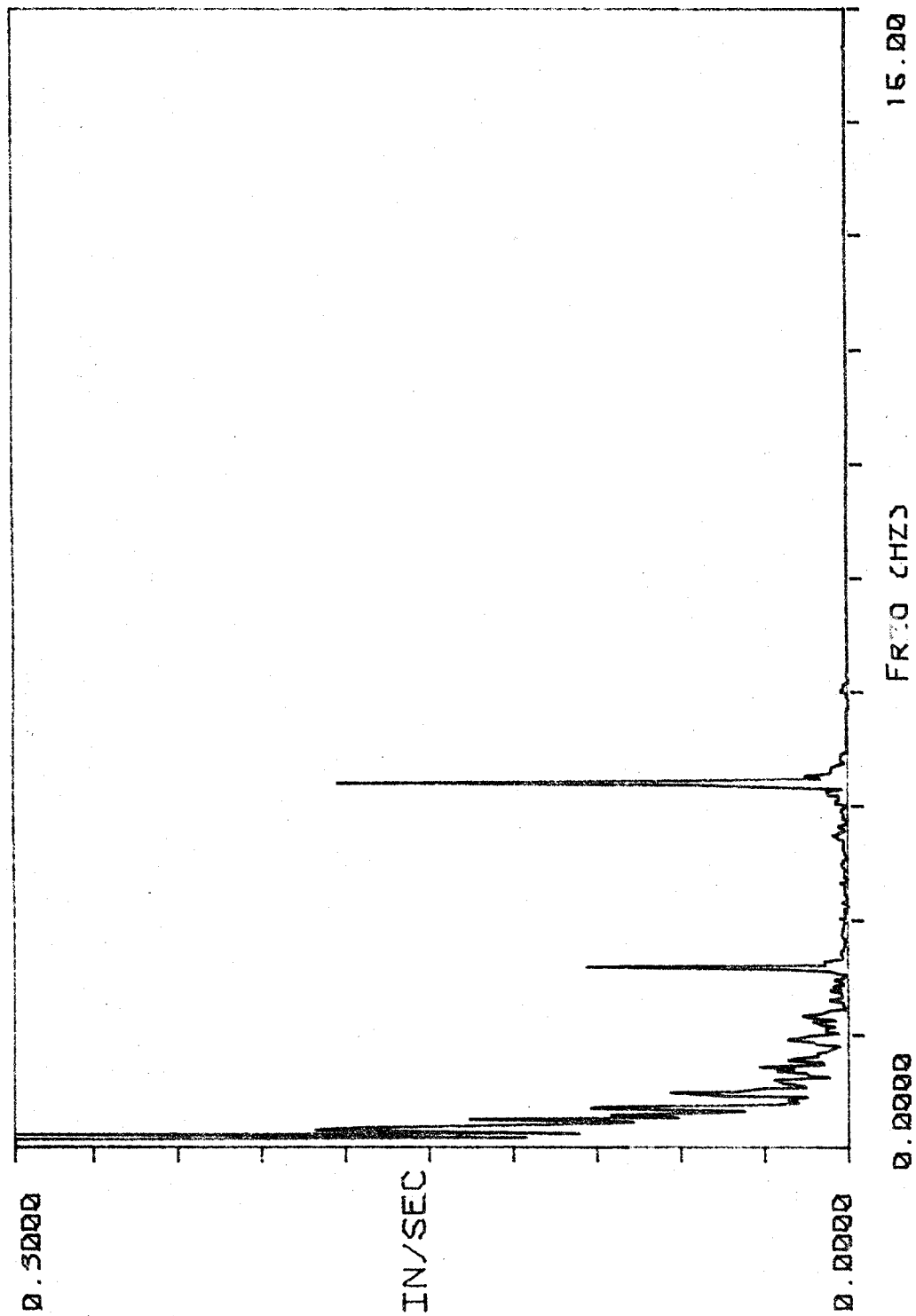
FIG. A1 ACCELERATION TIME HISTORY

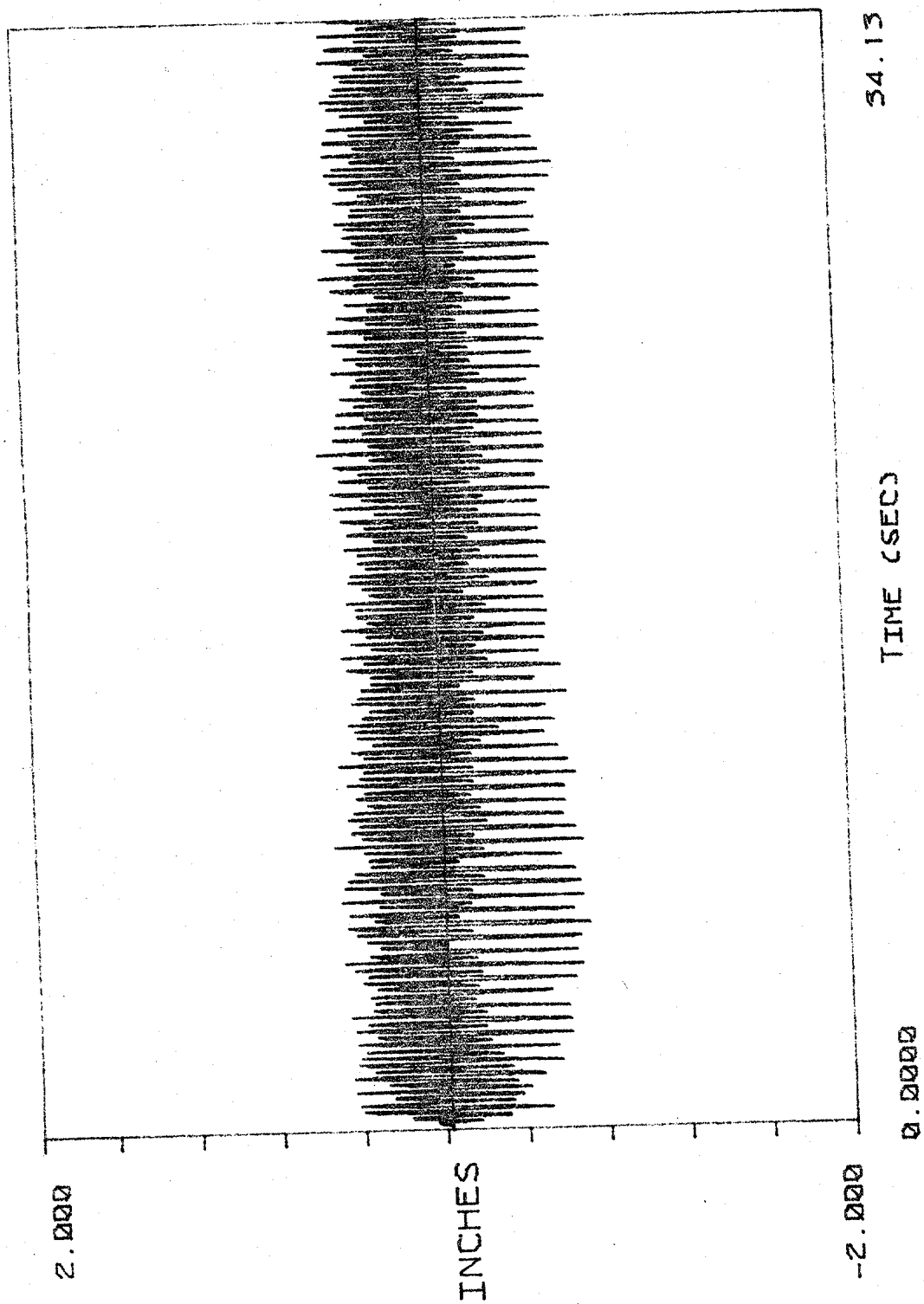FIG. A2 THEORETICAL FFT OF THE DISPLACEMENT

FIG. A3 DOUBLE-INTEGRATED DISPLACEMENT TIME HISTORY
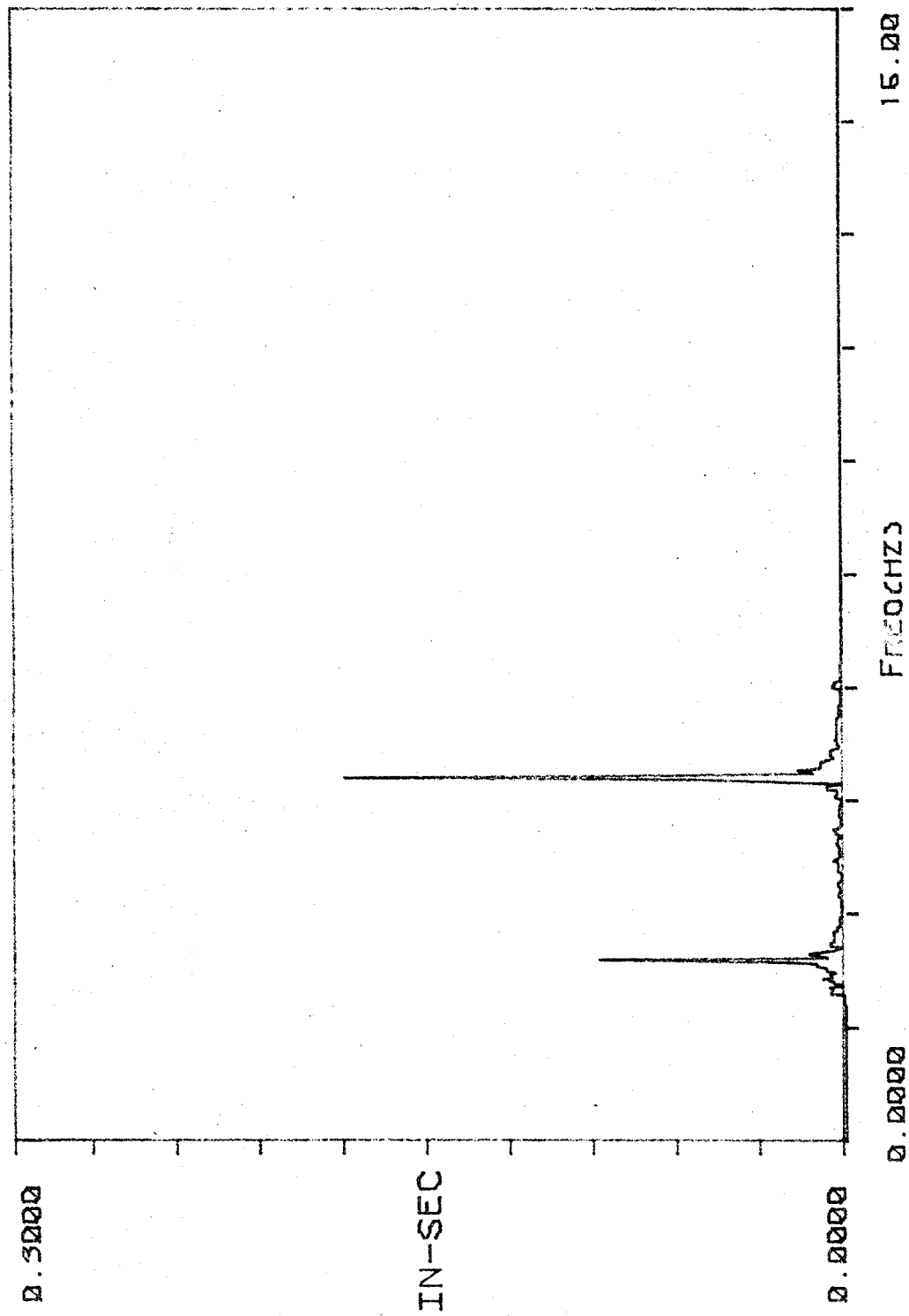
FIG. A4 FFT OF THE DOUBLE-INTEGRATED DISPLACEMENT

(1) PROGRAM IIR

RUN IIR
1. ENTER OUTPUT FILTER COEFFICIENT FILE NAME
    ?FILTER.DAT

2. ENTER ORDER OF THE FILTER(EVEN #)
    ?8

3. ENTER 0 FOR LOW AND HIGH PASS FILTER
    OR ENTER 1 FOR BAND PASS AND REJECT FILTER
    ?0

4. ENTER PASS BAND RIPPLE ATTENUATION W.R.T. 1
    ?0.01

5. ENTER SAMPLING FREQUENCY IN HZ
    30 HZ FOR CASTINE EXPERIMENT
    ?30

6. FOR LOWPASS : ENTER 0
    FOR HIGHPASS : ENTER PASSBAND FREQUENCY IN HZ
    FOR BANDPASS : ENTER FIRST PASSBAND FREQ IN HZ
    FOR BANDSTOP : ENTER SECOND PASSBAND FREQ IN HZ
    ?2.0

7. FOR LOWPASS : ENTER PASSBAND FREQ IN HZ
    FOR HIGHPASS : ENTER SAMPLING FREQ IN HZ
    FOR BANDPASS : ENTER SECOND PASSBAND FREQ IN HZ
    FOR BANDSTOP : ENTER FIRST PASSBAND FREQ IN HZ
    ?30

8. FOR LOWPASS OR HIGHPASS: ENTER POSITIVE STOPBAND FREQ
    OR ENTER NEGATIVE STOPBAND RIPPLE IN DB
    ****

78

FOR BANDPASS AND STOP : ENTER NEGATIVE STOPBAND RIPPLE IN DB
?1.7

(2) PROGRAM LLITG
RUN LLITG

1.   ENTER FILTER COEFFICIENTS FILE NAME
      ?FILTER.DAT

2.   ENTER # OF DATA POINTS
      ?1024

3.   ENTER SAMPLING FREQ(SAMPLES/SEC)
      ?30

4.   ENTER RAW DATA FILE NAME (BINARY DATA)
      ?C8031.RO3

5.   ENTER OUTPUT DISPLACEMENT FILE NAME (BINARY DATA)
      ?C8031.DO3

Description of the Program Input/Output Requirements

PROGRAM IIR:

1. FILTER.DAT is the output ASCII data file contaiing filter coefficients which is the input file to program LLITG.

2. Order of the filter which is discussed in Appendix 1-(4) in this example 8.

3. Choose correct one - 0 in this example for highpass filter.

4. e.g., for highpass filter in Figure 12,   is the passband ripple expressed as a decimal fraction less than 1.0 -0.01 in this example.

5. Sampling frequency in Hz = number of samples per second - 30 Hz in this example.

6. In the example for a highpass filter as in Figure 12, is the passband frequency, 2.0 Hz.

7. In this example for a highpass filter we enter 30 Hz, the sampling frequency.

8. For lowpass or highpass filter:
either enter stop-band frequency   as a positive number in Hz or
enter stop-band ripple   as a negative number in dB.
For band-pass or band-stop filter:
enter stop-band ripple   as a negative number in dB.
In this example of highpass filter, we enter stop-band frequency +1.7 Hz.

PROGRAM LLITG:

1. Enter name of output file from program IRR which contains the filter coefficients - FILTER.DAT in this example.

2. Number of data points in the acceleration time history -

1024 in this example.

3.　Sampling frequency in Hz - 30 Hz in this example.

4.　C8031.RO3 is an example input acceleration BINARY data file name.

5.　C8031.DO3 is an example output displacement BINARY data file name.

The displacement figures shown in this thesis were obtained from double integration of 1500 (50 sec) acceleration data points. Because of the transient effect of the filters (also integrators) on the beginning and ending parts of the data, 238 data points were discarded on both ends and a total of 1024 (34.14 sec) displacement data points were shown in those figures.

Program LLITG can integrate at most 2048 data points. For the 2 1/2 hour long records, as shown in Figures 25 through 28, modification of this program was required. The program was broken into individual steps as described in Chapter 3, section 5. In each step, the data was processed segment by segment. Because of the transient effect in the filters (also integrators), each segment was not processed independently of the next segment Careful linkage between segments was done by storing the ending of the previous segment, and using it as the beginning of the next segment, so that transients were eliminated in moving from one segment to the next.